POLITECNICO DI MILANO

Scuola di Ingegneria Industriale e dell'Informazione

Corso di Laurea Magistrale in Ingegneria Fisica

A Synchronously Pumped Ultrafast Optical Parametric Oscillator tunable from 1000 nm to 1400 nm

Relatore:

Prof. Giulio Cerullo

Correlatore:

Dott. Cosimo D'Andrea

Tesi di laurea di:

Francesco Crisafi

matr. 781272

Anno Accademico 2012/2013

Contents

List of Figures

List of Tables

Abstract in lingua italiana

Il campo della ottica non lineare si è sviluppato velocemente negli ultimi 50 anni, grazie anche alla scoperta di innovative tecniche di Phase Matching come il Quasi-Phase Matching (QPM). Gli *Optical Parametric Oscillators* (OPOs) sono il risultato di questo percorso e sono destinati a integrare le ordinarie sorgenti di luce laser, grazie alla loro versatilità e tunabilità. Questo progetto di tesi si propone di illustrare la realizzazione di un *Ultrafast Optical Parametric Oscillator* accordabile tra 1000nm e 1400nm: partendo dalla progettazione della cavità, passando attraverso la costruzione della sorgente fino ad arrivare alla sua applicazione. Questo progetto ha come principale motivazione quella di realizzare una sorgente accordabile nel visibile per misure di fotoluminescenza risolte in tempo. La progettazione di tale sorgente è stata realizzata in collaborazione con il gruppo di ricerca universitario della Heriot-Watt University di Edinburgo, specializzato nella realizzazione di *Ultrafast Optical Parametric Oscillators*. Al fine di apprendere tecniche di realizzazione e di costruzione di questo tipo di sorgente sono stato ospite presso il loro gruppo di ricerca per un breve periodo, collaborando direttamente con uno studente di dottorato del gruppo di ricerca di Derryck T. Reid. La sorgente è stata completamente realizzata nel polo di ricerca *Center for Nanoscience and Technology* (CNST) presso l'Istituto Italiano di Tecnologia (IIT).

Abstract

The field of nonlinear optics has grown rapidly over the last 50 years, thanks to the discovery of innovative techniques of Phase Matching such as Quasi-Phase Matching (QPM). The Optical Parametric Oscillators (OPOs) are the result of this trend and are intended to supplement the ordinary laser light sources, due to their versatility and tunability. This thesis project aims to illustrate the implementation of an Ultrafast Optical Parametric Oscillator tunable from 1000nm to 1400nm: starting from the design of the cavity, passing through the construction of the source until its application. This project has as its main motivation to realize a source tunable in the visible for time-resolved photoluminescence measurements. The design of this source has been realized in collaboration with a research group of the Heriot-Watt University in Edinburgh, specialized in the production of Ultrafast Optical Parametric Oscillators. In order to learn the techniques of design and construction of this type of source I visited as a guest their research center for a short time, working directly with a PhD student in the research group of Derryck T. Reid. The source has been fully implemented in the Center for Nanoscience and Technology (CNST) at the Italian Institute of Technology (IIT).

Chapter 1

Theoretical Foundations

In this chapter the origin and the meaning of the principal non-linear phenomena of second order will be discussed, with particular focus on those that are involved in the realization of the Optical Parametric Oscillator (OPO).

1.1   Pulse Theory and Description

Let us start from Maxwell's equations:

$$\nabla \cdot \mathbf{D} = \rho \tag{1.1}$$

$$\nabla \cdot \mathbf{B} = 0 \tag{1.2}$$

$$\nabla \times \mathbf{E} = -\frac{\partial \mathbf{B}}{\partial t} \tag{1.3}$$

$$\nabla \times \mathbf{B} = \mu_0 \left(\mathbf{J} + \frac{\partial \mathbf{D}}{\partial t} \right) \tag{1.4}$$

where $\mathbf{E}$ is the electric field vector, $\mathbf{D}$ is the electric displacement vector, $\mathbf{H}$ is the magnetic field vector and $\mathbf{B}$ is the magnetic induction vector. The quantities ρ and $\mathbf{J}$ are respectively the volume charge density and the electric current density of any external charges (not including any polarization

induced charges and currents). Furthermore it is important to remember the constitutive relations that link together the electric and magnetic field with their respective polarization and magnetization vectors:

$$\mathbf{D} = \epsilon_0 \mathbf{E} + \mathbf{P} \tag{1.5}$$

$$\mathbf{B} = \mu_0 \mathbf{H} + \mathbf{M} \tag{1.6}$$

In the following we will consider always media with negligible magnetization ($\mathbf{M} \cong 0$) as in the case of paramagnetic and diamagnetic materials. We will also assume that there are no free charges ($\rho = 0$) and currents ($\mathbf{J} = 0$). In this case the equations simplify to:

$$\nabla \cdot \mathbf{D} = 0 \tag{1.7}$$

$$\nabla \cdot \mathbf{B} = 0 \tag{1.8}$$

$$\nabla \times \mathbf{E} = -\frac{\partial \mathbf{B}}{\partial t} \tag{1.9}$$

$$\nabla \times \mathbf{B} = \mu_0 \frac{\partial \mathbf{D}}{\partial t} \tag{1.10}$$

Taking the curl of both sides of Equation 1.9, we obtain:

$$\nabla \times \nabla \times \mathbf{E} = -\frac{\partial}{\partial t} (\nabla \times \mathbf{B}) = -\mu_0 \frac{\partial^2 \mathbf{D}}{\partial t^2} \tag{1.11}$$

Recalling that for a vector ν applies $\nabla \times \nabla \times \nu = \nabla (\nabla \cdot \nu) - \nabla^2 \nu$, we obtain the wave equation:

$$\nabla^2 \mathbf{E} = \mu_0 \epsilon_0 \frac{\partial^2 \mathbf{E}}{\partial t^2} + \mu_0 \frac{\partial^2 \mathbf{P}}{\partial t^2} \tag{1.12}$$

remembering Equation 1.5 and Equation 1.7.

Equation 1.12 is a vector equation. We first make the **scalar approximation**[2], by considering a linearly polarized pulse propagating in the z

direction and considering only one component E of the electric field vector:

$$\frac{\partial^2 E}{\partial z^2} + \nabla_T^2 E = \mu_0 \epsilon_0 \frac{\partial^2 E}{\partial t^2} + \mu_0 \frac{\partial^2 P}{\partial t^2} \tag{1.13}$$

where $\nabla_T^2 E = \frac{\partial^2 E}{\partial x^2} + \frac{\partial^2 E}{\partial y^2}$ is the so-called transverse Laplacian operator. We further make the **plane wave approximation**[2], by assuming a plane wave and neglecting any transverse variation of the electric field:

$$\frac{\partial^2 E}{\partial z^2} - \frac{1}{c_0^2} \frac{\partial^2 E}{\partial t^2} = \mu_0 \frac{\partial^2 P}{\partial t^2} \tag{1.14}$$

where $c_0 = \frac{1}{\sqrt{\epsilon_0 \mu_0}}$ is the speed of light in vacuum. Equation 1.14 already allows a first physical insight into the propagation of an electro-magnetic wave into a medium with polarization P. The polarization is on the right hand side of the equation, thus acts as a driving term for the electric field, modifying it during propagation.

Let us now consider a plane wave of the form:

$$E(z, t) = A_1(z, t) cos\left[\omega_0 t - k_0 z + \phi(z, t)\right] \tag{1.15}$$

where A_1 is the field envelope (a real function), ω_0 is the carrier frequency
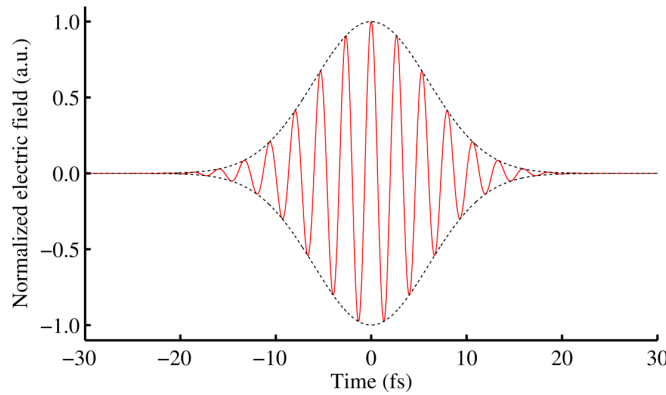
Figure 1.1: The real component of the electric field representing a Gaussian pulse with $10 fs$ duration at $\lambda_0 = 0.8 \mu m$. The dashed line represents the envelope function that is modulated by the underlying carrier wave, shown in red.

and $k_0 = \frac{\omega_0}{c(\omega_0)} = \frac{\omega_0 n(\omega_0)}{c_0}$ is the wave-number in vacuum. It is often more convenient to rewrite Equation 1.15 as:

$$E(z,t) = Re\left\{A(z,t)exp\left[i\left(\omega_0 t - k_0 z\right)\right]\right\} \qquad (1.16)$$

where $A(z,t)$ is the complex field envelope. In the following we will avoid the expression $Re\left\{...\right\}$ and write the electric field as:

$$E(z,t) = A(z,t)exp\left[i\left(\omega_0 t - k_0 z\right)\right] \qquad (1.17)$$

It is however important to remember that the electric field is always a real quantity. Note that an alternative expression for Equation 1.16 is:

$$E(z,t) = \frac{1}{2}\left\{A(z,t)exp\left[i\left(\omega_0 t - k_0 z\right)\right] + A^*(z,t)exp\left[-i\left(\omega_0 t - k_0 z\right)\right]\right\} =$$
$$\frac{1}{2}\left\{A(z,t)exp\left[i\left(\omega_0 t - k_0 z\right)\right] + c.c.\right\}$$
$$(1.18)$$

Similarly, the polarization can be written as[2]:

$$P(z,t) = p(z,t)exp\left[i\left(\omega_0 t - k_p z\right)\right] \qquad (1.19)$$

where we have assumed for generality that the wave-vector of the polarization k_p is different from that of the field k_0. The polarization is a function of the incident electric field and can be decomposed in the sum of a linear (P_L) and a non-linear (P_{NL}) component:

$$P(z,t) = P_L(z,t) + P_{NL}(z,t) \qquad (1.20)$$

For the remainder of this section we will consider only the linear component:

$$P(z,t) = P_L(z,t) = p_L(z,t)\left[i\left(\omega_0 t - k_0 z\right)\right] \qquad (1.21)$$

and solve the equation:

4

$$\frac{\partial^2 E}{\partial z^2} - \frac{1}{c_0^2}\frac{\partial^2 E}{\partial t^2} = \mu_0 \frac{\partial^2 P_L}{\partial t^2} \tag{1.22}$$

Eq. 1.22 is more easily solved in the frequency domain, by introducing the Fourier transform:

$$\tilde{E}(z,\omega) = \mathcal{F}\left[E(z,t)\right] = \int_{-\infty}^{+\infty} E(z,t)exp\left(-i\omega t\right)dt \tag{1.23}$$

It can be shown that the Fourier transform of E and P_L are[2]:

$$\tilde{E}(z,\omega) = \tilde{A}(z,\omega - \omega_0)exp\left(-ik_0 z\right) \tag{1.24}$$

$$\tilde{P}_L(z,\omega) = \tilde{p_L}(z,\omega - \omega_0)exp\left(-ik_0 z\right) \tag{1.25}$$

where $\tilde{A}(z,\omega) = \mathcal{F}\left[A(z,t)\right]$. By taking the Fourier transform of Eq. 1.22 and recalling the derivative rule for the Fourier transform[2]:

$$\mathcal{F}\left[\frac{d^n F(t)}{dt^n}\right] = (i\omega)^n \tilde{F}(\omega) \tag{1.26}$$

we obtain:

$$\frac{\partial^2 \tilde{E}}{\partial z^2} + \frac{\omega^2}{c_0^2}\tilde{E} = -\mu_0\omega^2 \tilde{P}_L \tag{1.27}$$

It is possible to express the derivatives with respect to the longitudinal propagation coordinate z as follows:

$$\frac{\partial \tilde{E}}{\partial z} = \left(\frac{\partial \tilde{A}}{\partial z} - ik_0\tilde{A}\right)exp\left(-ik_0 z\right) \tag{1.28}$$

$$\frac{\partial^2 \tilde{E}}{\partial z^2} = \left(\frac{\partial^2 \tilde{A}}{\partial z^2} - 2ik_0\frac{\partial \tilde{A}}{\partial z} - k_0^2\tilde{A}\right)exp\left(-ik_0 z\right) \tag{1.29}$$

By plugging Eq. 1.29 into Eq. 1.27 we obtain:

$$\frac{\partial^2 \tilde{A}}{\partial z^2} - 2ik_0\frac{\partial \tilde{A}}{\partial z} - k_0^2\tilde{A} + \frac{\omega^2}{c_0^2}\tilde{A} = -\mu_0\omega^2\tilde{p_L} \tag{1.30}$$

Using now the **Slowly Varying Envelope Approximation (SVEA)**[2], which consists in assuming that $\frac{\partial^2 \tilde{A}}{\partial z^2} << k_0 \frac{\partial \tilde{A}}{\partial z}$, this corresponds to neglecting variations of the envelope over propagation lengths of the order of the wavelength and breaks down only for extreme focusing (down to the diffraction limit). With this assumption it can be written that:

$$-2ik_0 \frac{\partial \tilde{A}}{\partial z} - k_0^2 \tilde{A} + \frac{\omega^2}{c_0^2} \tilde{A} = -\mu_0 \omega^2 \tilde{p_L} \tag{1.31}$$

To continue, an expression of $\tilde{p_L}(\omega)$ is needed. Just recalling that for a monochromatic wave:

$$\tilde{P}_L(\omega) = \epsilon_0 \chi^{(1)}(\omega) \tilde{E}(\omega) \tag{1.32}$$

where $\chi^{(1)}(\omega)$ is the linear (first-order) dielectric susceptibility. By recalling the definition of linear refractive index $n_L(\omega) = \sqrt{\left(1 + \chi^{(1)}(\omega)\right)}$, we obtain:

$$\tilde{p_L}(\omega) = \epsilon_0 \left[n_L^2(\omega) - 1\right] \tilde{A}(\omega) \tag{1.33}$$

We finally obtain:

$$-2ik_0 \frac{\partial \tilde{A}}{\partial z} - k_0^2 \tilde{A} + \frac{\omega^2}{c_0^2} \tilde{A} = -\mu_0 \epsilon_0 \omega^2 \left[n_L^2(\omega) - 1\right] \tilde{A} = -\frac{\omega^2}{c_0^2} \left[n_L^2(\omega) - 1\right] \tilde{A} \tag{1.34}$$

which simplifies to:

$$2ik_0 \frac{\partial \tilde{A}}{\partial z} = \left[k^2(\omega) - k_0^2\right] \tilde{A} \tag{1.35}$$

with $k(\omega) = \frac{\omega}{c_0} n(\omega)$. In a dispersive medium, the refractive index is a function of frequency, and the wave-vector thus becomes a nonlinear function of ω. It is possible to write that[2]:

$$k^2(\omega) - k_0^2 = [k(\omega) - k_0][k(\omega) + k_0] \cong 2k_0[k(\omega) - k_0] \tag{1.36}$$

By a Taylor expansion of $k(\omega)$ around ω_0:

$$k(\omega) = k_0 + \left(\frac{dk}{d\omega}\right)_{\omega_0} (\omega - \omega_0) + \frac{1}{2} \left(\frac{d^2k}{d\omega^2}\right)_{\omega_0} (\omega - \omega_0)^2 + \frac{1}{6} \left(\frac{d^3k}{d\omega^3}\right)_{\omega_0} (\omega - \omega_0)^3 + ...$$
$$(1.37)$$

Usually an expansion up to the third order (or to the second order for moderate pulse bandwidths) is sufficient. By substituting Eq. 1.36 and Eq. 1.37 into Eq. 1.35, we obtain:

$$i\frac{\partial \tilde{A}(\omega - \omega_0)}{\partial z} \cong k_0' (\omega - \omega_0) \tilde{A} + \frac{1}{2} k_0'' (\omega - \omega_0)^2 \tilde{A} + \frac{1}{6} k_0''' (\omega - \omega_0)^3 \tilde{A} \quad (1.38)$$

where $k_0' = \left(\frac{dk}{d\omega}\right)_{\omega_0} = \frac{1}{v_{g0}}$, v_{g0} is the group velocity of the carrier frequency; $k_0'' = \left(\frac{d^2k}{d\omega^2}\right)_{\omega_0} = GVD$ is known as **Group Velocity Dispersion (GVD)** and $k_0''' = \left(\frac{d^3k}{d\omega^3}\right)_{\omega_0} = TOD$ is the **Third Order Dispersion (TOD)**. It is possible now to transform Eq. 1.38 back to the time domain. From Eq. 1.26 the following rule can be derived[2]:

$$\mathcal{F}^{-1}\left[\omega^n \tilde{F}(\omega)\right] = (-i)^n \frac{d^n F(t)}{dt^n} \quad (1.39)$$

Obtaining:

$$\frac{\partial A(z,t)}{\partial z} + \frac{1}{v_{g0}} \frac{\partial A}{\partial t} - \frac{i}{2} k_0'' \frac{\partial^2 A}{\partial t^2} + \frac{1}{6} k_0''' \frac{\partial^3 A}{\partial t^3} = 0 \quad (1.40)$$

Eq. 1.40 can be simplified by changing to a temporal frame of reference moving with the group velocity of the carrier wave: $z' = z, \tau = t - \frac{z}{v_{g0}}$, obtaining:

$$\begin{aligned}
\frac{\partial}{\partial t} &= \frac{\partial}{\partial z'}\frac{\partial z'}{\partial t} + \frac{\partial}{\partial \tau}\frac{\partial \tau}{\partial t} = \frac{\partial}{\partial \tau} \\
\frac{\partial^n}{\partial t^n} &= \frac{\partial^n}{\partial \tau^n} \\
\frac{\partial}{\partial z} &= \frac{\partial}{\partial z'}\frac{\partial z'}{\partial z} + \frac{\partial}{\partial \tau}\frac{\partial \tau}{\partial z} = \frac{\partial}{\partial z} - \frac{1}{v_{g0}}\frac{\partial}{\partial \tau}
\end{aligned} \quad (1.41)$$

In this new frame of reference Eq. 1.40 becomes:

$$\frac{\partial A}{\partial z'} - \frac{i}{2}k_0''\frac{\partial^2 A}{\partial \tau^2} + \frac{1}{6}k_0'''\frac{\partial^3 A}{\partial \tau^3} = 0 \qquad (1.42)$$

In the case, often satisfied in practice, in which one can assume $k_0''' \cong 0$, Eq. 1.42 further simplifies to:

$$\frac{\partial A}{\partial z'} - \frac{i}{2}k_0''\frac{\partial^2 A}{\partial \tau^2} = 0 \qquad (1.43)$$

Eq. 1.43, also known as the parabolic equation, captures the main physics of linear propagation of ultrashort pulses in dispersive media. Let us study the propagation of a pulse, with a known envelope at $z = 0$, $A(0,t) = A_0(t)$.

Starting with the simplified case of a non-dispersive medium, in which the refractive index is constant with frequency: $n(\omega) = n(\omega_0) = const$. In this case $k(\omega) = \frac{\omega}{c_0}n(\omega_0)$ is a linear function of frequency, and $k_0'' = 0$. We then have: $\frac{\partial A(z,\tau)}{\partial z} = 0$ which gives $A(L,\tau) = const = A_0(\tau) = A_0\left(t - \frac{L}{v_{g0}}\right)$. We thus have a pulse that moves with the group velocity of the carrier frequency (so that its peak position shifts linearly with time) but maintains its shape unaltered. Note that, strictly speaking, only the vacuum is a non-dispersive medium. The spectrum of the pulse after propagation acquires a linear phase:

$$\tilde{A}\left(L,\omega\right) = \tilde{A}\left(0,\omega\right)exp\left(-i\frac{L}{v_{g0}}\omega\right) = \tilde{A}\left(0,\omega\right)exp\left(-i\tau_{g0}\omega\right) \qquad (1.44)$$

where $\tau_{g0} = \frac{L}{v_{g0}}$ is called the **group delay** of the carrier frequency, and is the delay of the pulse envelope upon propagation in a non-dispersive medium.

Turning now to a dispersive medium; Eq. 1.43 can be solved by taking a Fourier transform with respect to time:

$$\frac{\partial \tilde{A}\left(z,\omega\right)}{\partial z} + \frac{i}{2}\omega^2 k_0'' \tilde{A} = 0 \qquad (1.45)$$

Note that now we are working in the so-called base band[2], i.e. with the envelope A which is a slowly varying function of time. Eq. 1.45 can be easily solved by separation of variables:

$$\tilde{A}\left(L,\omega\right) = \tilde{A}\left(0,\omega\right) exp\left(-\frac{i}{2}D_2\omega^2\right) \qquad (1.46)$$

where it has been defined $D_2 = k_0''L$ as the **second order dispersion (or Group Delay Dispersion, GDD)**[2]. It should be noted that, since the phase shift induced by propagation through a length L can be expressed as $\phi(\omega) = k(\omega)L$, one can write $D_2 = \left(\frac{d^2\phi}{d\omega^2}\right)_{\omega_0}$. Now going back to the time domain:

$$A\left(L,t\right) = \frac{1}{2\pi}\int_{-\infty}^{+\infty}\tilde{A}\left(0,\omega\right) exp\left(-\frac{i}{2}D_2\omega^2\right) exp\left(i\omega t\right) d\omega \qquad (1.47)$$

Eq. 1.46 can be numerically solved for any input pulse; it is possible to see that the effect of propagation in a dispersive medium is to add to the spectrum a **quadratic phase**[2]. An analytical solution of 1.47 is possible only in the special case of a Gaussian pulse shape:

$$A_0\left(\tau\right) = A_0 exp\left(-\frac{\tau^2}{2\tau_p^2}\right) \qquad (1.48)$$

This pulse shape, although it does not realistically represent many ultrashort laser pulses, is amenable to analytical calculation, because the Fourier transform of a Gaussian function is also Gaussian. The parameter τ_p defines the pulse duration; for an ultrashort pulse, in particular, one usually specifies the intensity Full Width at Half Maximum (FWHM), which is given by:

$$\tau_{FWHM} = \sqrt{2ln\left(2\right)}\tau_p \qquad (1.49)$$

By recalling that:

$$\mathcal{F}\left[exp\left(-at^2\right)\right] = \sqrt{\frac{\pi}{a}}exp\left(-\frac{\omega^2}{4a}\right) \qquad (1.50)$$

And putting $a = 1/2\tau_p^2$ we obtain:

$$\tilde{A}_0\left(\omega\right) = \sqrt{2\pi}\tau_p A_0 exp\left(-\frac{\tau_p^2\omega^2}{2}\right) \tag{1.51}$$

and, after propagation:

$$\tilde{A}\left(L,\omega\right) = \sqrt{2\pi}\tau_p A_0 exp\left[-\frac{\tau_p^2}{2}\omega^2\left(1 + i\frac{D_2}{\tau_p^2}\right)\right] \tag{1.52}$$

Transforming back to the time domain, we obtain:

$$
\begin{aligned}
A\left(L,\tau\right) =& \frac{A_0\tau_p}{\sqrt{\tau_p^2 + iD_2}} exp\left[-\frac{\tau^2}{2\left(\tau_p^2 + iD_2\right)}\right] = \\
& \frac{A_0\tau_p}{\sqrt{\tau_p^2 + iD_2}} exp\left(-\frac{\tau^2}{2\tau_{out}^2}\right) exp\left[i\phi\left(\tau\right)\right]
\end{aligned}
\tag{1.53}
$$

where:

$$\tau_{out}^2 = \tau_p^2 + \frac{D_2^2}{\tau_p^2} = \tau_p^2\left[1 + \left(\frac{D_2}{\tau_p^2}\right)^2\right] \tag{1.54}$$

and:

$$\phi\left(\tau\right) = \frac{D_2\tau^2}{2\left(\tau_p^4 + D_2^2\right)} \tag{1.55}$$

By recalling that $D_2 = k_0'' L$ and defining a "**dispersion length**" $L_D = \frac{\tau_p^2}{k_0''}$, Eq. 1.54 can be rewritten as:

$$\tau_{out} = \tau_p\sqrt{1 + \left(\frac{L}{L_D}\right)^2} \tag{1.56}$$

Eq. 1.56 already allows a physical insight into the mechanism of dispersive pulse broadening. For short propagation lengths, $L << L_D$, the pulse-width remains basically unchanged upon propagation, while for long propagation, $L >> L_D$, a linear broadening with distance appears, $\tau_{out} = \frac{\tau_p}{L_D}L$.

Note that the temporal spreading of the Gaussian pulse due to dispersion has the same expression as the spatial spreading of a Gaussian beam due to diffraction[2]:

$$w\left(z\right) = w_0\sqrt{1 + \left(\frac{z}{z_R}\right)^2} \tag{1.57}$$

where the Rayleigh range, defined as $z_R = \frac{n\pi w_0^2}{\lambda}$, plays a similar role to the dispersion length L_D.

Let's now consider the time-dependent temporal phase. By recalling that the ultrashort pulse is written as:

$$E\left(z, \tau\right) = |A\left(z, \tau\right)|\, exp\left[i\left(\omega_0\tau - k_0 z + \phi\left(\tau\right)\right)\right] \tag{1.58}$$

The instantaneous pulse frequency becomes:

$$\omega_i\left(\tau\right) = \omega_0 + \frac{d\phi}{d\tau} = \omega_0 + \frac{2D_2}{2\left(\tau_p^4 + D_2^2\right)} \tag{1.59}$$

The frequency is thus not constant, but displays a linear temporal variation, or **"chirp"**. In particular, for $D_2 > 0$, the frequency increases with time ("positive chirp" or "up-chirp"), while for $D_2 < 0$, the frequency decreases with time ("negative chirp" or "down-chirp").
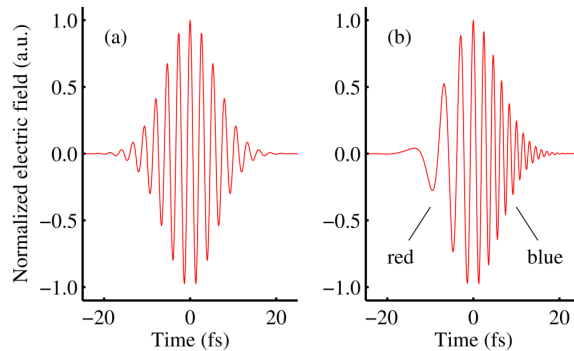
Figure 1.2: A $10fs$ pulse (a) before and (b) after positive dispersive broadening. Longer blue frequencies are delayed relative to the shorter red frequencies.

To understand this behaviour, let's recall that: $D_2 \propto \frac{d}{d\omega}\frac{dk}{d\omega} = \frac{d}{d\omega}\left(\frac{1}{v_g(\omega)}\right)$ so that $D_2 > 0$ means that v_g decreases with frequency (and viceversa for $D_2 < 0$). For $D_2 > 0$, therefore, the higher frequencies (blue components of the spectrum) will move at lower speed with respect to the lower frequencies (red components of the spectrum) and get delayed. The pulse thus acquires an up-chirp. The opposite holds for the case of a down-chirp.

To further understand this point, let's express the laser pulse like an inverse Fourier transform (or Fourier integral)[2]:

$$E(t) = \frac{1}{2\pi}\int_{-\infty}^{+\infty}\left|\tilde{E}(\omega)\right|exp\left[-i\phi(\omega)\right]exp\left(i\omega t\right)d\omega \qquad (1.60)$$

Let us now slice from the pulse spectrum a narrow interval of frequencies around a given frequency $\bar{\omega}$:

$$E_{\bar{\omega}}(t) = \frac{1}{2\pi}\int_{\bar{\omega}-\Delta\omega}^{\bar{\omega}+\Delta\omega}\left|\tilde{E}(\omega)\right|exp\left[-i\phi(\omega)\right]exp\left(i\omega t\right)d\omega \qquad (1.61)$$

By expanding $\phi(\omega)$ around $\bar{\omega}$ it is possible to write that:

$$E_{\bar{\omega}}(t) = \frac{1}{2\pi}exp\left(-i\bar{\omega}t\right)\int_{\bar{\omega}-\Delta\omega}^{\bar{\omega}+\Delta\omega}\left|\tilde{E}(\omega)\right|exp\left[-i\phi(\bar{\omega}) - i\left(\frac{d\phi}{d\omega}\right)_{\bar{\omega}}(\omega - \bar{\omega})\right]exp\left[i(\omega - \bar{\omega})t\right]d\omega =$$
$$\frac{1}{2\pi}exp\left[i(\bar{\omega}t - \phi(\bar{\omega}))\right]\int_{\bar{\omega}-\Delta\omega}^{\bar{\omega}+\Delta\omega}\left|\tilde{E}(\omega)\right|exp\left[i(\omega - \bar{\omega})\left(t - \left(\frac{d\phi}{d\omega}\right)_{\bar{\omega}}\right)\right]d\omega \qquad (1.62)$$

One can easily see that the r.h.s. of the equation is non-vanishing only when the argument of the exponential is zero, i.e. when:

$$t = \tau_g(\bar{\omega}) = \left(\frac{d\phi}{d\omega}\right)_{\bar{\omega}}$$

The **group delay** τ_g is thus the relative arrival time of a given frequency wave-packet within the pulse. By a Taylor expansion of the spectral phase:

$$\phi\left(\omega\right) = \phi\left(\omega_0\right) + \left(\frac{d\phi}{d\omega}\right)_{\omega_0}\left(\omega - \omega_0\right) + \frac{1}{2}\left(\frac{d^2\phi}{d\omega^2}\right)_{\omega_0}\left(\omega - \omega_0\right)^2 + \frac{1}{6}\left(\frac{d^3\phi}{d\omega^3}\right)_{\omega_0}\left(\omega - \omega_0\right)^3 + ... =$$

$$\phi\left(\omega_0\right) + \tau_{g0}\left(\omega - \omega_0\right) + \frac{1}{2}D_2\left(\omega - \omega_0\right)^2 + \frac{1}{6}D_3\left(\omega - \omega_0\right)^3 + ...$$

$$(1.63)$$

where $D_3 = \left(\frac{d^3\phi}{d\omega^3}\right)_{\omega_0}$ is called **third-order dispersion (TOD)**. One can thus write:

$$\tau_g\left(\omega\right) = \frac{d\phi\left(\omega\right)}{d\omega} = \tau_{g0} + D_2\left(\omega - \omega_0\right) + \frac{1}{2}D_3\left(\omega - \omega_0\right)^2 + ... \qquad (1.64)$$

Eq. 1.64 shows that for $D_2 = D_3 = 0$ all the frequency components of the pulse arrive simultaneously, so that it is called Transform-Limited (TL), while in all other cases the different frequency components arrive at different times and the pulse becomes chirped. In particular, if the D_2 term is dominant (quadratic chirp) then the group delay varies linearly with frequency, meaning that the instantaneous frequency is swept within the pulse envelope (from red to blue for positive chirp and from blue to red for negative chirp).

1.2 Elements of Non-Linear Optics

Starting with the equation:

$$\frac{\partial^2 E}{\partial z^2} - \frac{1}{c_0^2}\frac{\partial^2 E}{\partial t^2} = \mu_0\frac{\partial^2 P_L}{\partial t^2} + \mu_0\frac{\partial^2 P_{NL}}{\partial t^2} \qquad (1.65)$$

where:

$$P_{NL}\left(z, t\right) = p_{NL}\left(z, t\right) exp\left[i\left(\omega_0 t - k_p z\right)\right] \qquad (1.66)$$

having emphasized that the wave-number k_p of the nonlinear polarization at ω_0 is different from that of the electric field. The second derivative of the nonlinear polarization can be expressed as:

$$\frac{\partial^2 P_{NL}}{\partial t^2} = \left(\frac{\partial^2 p_{NL}}{\partial t^2} + 2i\omega_0 \frac{\partial p_{NL}}{\partial t} - \omega_0^2 p_{NL} \right) exp\left[i\left(\omega_0 t - k_p z \right) \right] \qquad (1.67)$$

Now making the approximation that the envelope p_{NL} varies slowly over the timescale of an optical cycle[2], so that:

$$\frac{\partial^2 p_{NL}}{\partial t^2}, \omega_0 \frac{\partial p_{NL}}{\partial t} << \omega_0^2 p_{NL} \qquad (1.68)$$

Equation 1.67 then becomes:

$$\frac{\partial^2 P_{NL}}{\partial t^2} \cong -\omega_0^2 p_{NL} exp\left[i\left(\omega_0 t - k_p z \right) \right] \qquad (1.69)$$

By plugging 1.69 into Eq. 1.65 and solving it in the same way it was reported in the previous section, we obtain[2]:

$$-2ik_0 \frac{\partial A}{\partial z} - 2\frac{ik_0}{v_{g0}} \frac{\partial A}{\partial t} - k_0 k_0'' \frac{\partial^2 A}{\partial t^2} = -\mu_0 \omega_0^2 p_{NL} exp\left[-i\Delta k z \right] \qquad (1.70)$$

where $\Delta k = k_p - k_0$ is the so-called "**wave-vector mismatch**" between the nonlinear polarization and the field. Eq. 1.70, recalling that $\omega_0 / k_0 = c_0 / n\left(\omega_0 \right)$, can be rewritten as:

$$\frac{\partial A}{\partial z} + \frac{1}{v_{g0}} \frac{\partial A}{\partial t} - \frac{i}{2} k_0'' \frac{\partial^2 A}{\partial t^2} = -i\frac{\mu_0 \omega_0 c_0}{2n_0} p_{NL} exp\left[-i\Delta k z \right] \qquad (1.71)$$

In this work we will focus on the second order non-linear optics, the most significant process involved in the Optical Parametric Oscillator behavior.

1.2.1 Nonlinear susceptibility

When light propagates through a material the electrons and atoms within it react to the electromagnetic fields of the wave, producing a change in the spatial and temporal distribution of electrical charges. The field causes small displacements of the valance electrons from their normal orbits, perturbations

which create electric dipoles that are manifested as the electric polarization of the medium. For small field strengths (such as an unfocused, low energy laser beam) this electric polarization $P(\omega)$ is proportional to the electric field strength $E(\omega)$, expressed as:

$$P(\omega) = \epsilon_0 \chi^{(1)} E(\omega) \tag{1.72}$$

For intense electric fields a nonlinear polarization of the medium takes place, described as a power series expansion of Equation 1.72 and often written as:

$$P(\omega) = \epsilon_0 \left[\chi^{(1)} E(\omega) + \chi^{(2)} E^2(\omega) + \chi^{(3)} E^3(\omega) + ... \right] \tag{1.73}$$

where $\chi^{(2)}$ and $\chi^{(3)}$ are the second-order and third-order nonlinear susceptibilities respectively.

Optical field interactions involving the $\chi^{(2)}$ non-linearity are phase-only, with no photon energy being absorbed into the medium. This makes $\chi^{(2)}$ nonlinear processes appealing as they require no cooling and can be highly efficient. While all transparent materials display first- and third-order nonlinear susceptibility, second-order effects are only observed in non-centrosymmetric crystals[2]. Such nonlinear crystals can be used in power-scalable processes that are limited only by the material properties of the crystal, such as the damage threshold, hygroscopicity and photo-refraction.

The second-order nonlinear susceptibility can be exploited to produce a number of nonlinear interactions. A formal derivation of these processes will be given in the next section; however a more general outline will be given first here. The most common application of the $\chi^{(2)}$ non-linearity is to facilitate frequency mixing between two electromagnetic waves to produce an interfering field E, given by:

$$E(t) = \frac{1}{2} \left[A_1 e^{i(\omega_1 t - k_1 z)} + A_2 e^{i(\omega_2 t - k_2 z)} + c.c. \right] \tag{1.74}$$

By plugging Eq. 1.74 in $P_{NL} = \epsilon_0 \chi^{(2)} E^2(t)$, we obtain:

$$
\begin{aligned}
P_{NL} =& \frac{\epsilon_0 \chi^{(2)}}{4} \left(A_1^2 e^{i(2\omega_1 t - k_1 z)} + A_2^2 e^{i(2\omega_2 t - k_2 z)} + c.c. \right) \\
&+ \frac{\epsilon_0 \chi^{(2)}}{4} \left(2 A_1 A_2 e^{i[(\omega_1 + \omega_2)t - (k_1 + k_2)z]} + c.c. \right) \\
&+ \frac{\epsilon_0 \chi^{(2)}}{4} \left(2 A_1^* A_2 e^{i[(\omega_2 - \omega_1)t - (k_2 - k_1)z]} + c.c. \right) \\
&+ \frac{\epsilon_0 \chi^{(2)}}{4} \left(2 A_1 A_1^* + 2 A_2 A_2^* \right)
\end{aligned}
\tag{1.75}
$$

Exiting the non-linear medium there are the following fields:

- the incident fields at ω_1 and ω_2

- the second-harmonic generation of the two fields: $2\omega_1$ and $2\omega_2$ (SHG)

- the sum-frequency generation: $\omega_1 + \omega_2$ (SFG)

- the difference-frequency generation: $\omega_2 - \omega_1$ (DFG or OPA)

- the DC polarization component known as electro-optic rectification (EOR), a process exploited in the field of terahertz generation

Which of these phenomena will be efficient is selected by the **Phase-Matching Condition**:

$$
\Delta k = k_p - k_0
$$

1.2.2 Second Order Non-Linear Optics

Three-Wave Mixing

Let's consider the superposition of three fields, at frequencies ω_1, ω_2 and ω_3:

$$
\begin{aligned}
E(z, t) =& \frac{1}{2} A_1(z, t) \, exp \left[i \left(\omega_1 t - k_1 z \right) \right] \\
&+ \frac{1}{2} A_2(z, t) \, exp \left[i \left(\omega_2 t - k_2 z \right) \right] \\
&+ \frac{1}{2} A_3(z, t) \, exp \left[i \left(\omega_3 t - k_3 z \right) \right] + \frac{1}{2} c.c.
\end{aligned}
\tag{1.76}
$$

satisfying the condition:

$$\omega_1 + \omega_2 = \omega_3 \tag{1.77}$$

impinging on a medium with a second order nonlinear response:

$$P_{NL}(z,t) = \epsilon_0 \chi^{(2)} E^2(z,t) \tag{1.78}$$

Such a situation is known as "**nonlinear second-order parametric interaction**" and corresponds to an exchange of energy between the three fields by means of the second order non-linearity. The nonlinear polarization will contain three components at frequencies ω_1, ω_2 and ω_3. Given by[2]:

$$
\begin{aligned}
P_{NL}^1(z,t) &= \frac{\epsilon_0 \chi^{(2)}}{2} A_2^* A_3 exp\left\{i\left[(\omega_3 - \omega_2)t - (k_3 - k_2)z\right]\right\} + c.c. \\
P_{NL}^2(z,t) &= \frac{\epsilon_0 \chi^{(2)}}{2} A_1^* A_3 exp\left\{i\left[(\omega_3 - \omega_1)t - (k_3 - k_1)z\right]\right\} + c.c. \\
P_{NL}^3(z,t) &= \frac{\epsilon_0 \chi^{(2)}}{2} A_1 A_2 exp\left\{i\left[(\omega_1 + \omega_2)t - (k_1 + k_2)z\right]\right\} + c.c.
\end{aligned}
\tag{1.79}
$$

Obviously there are other terms on P_{NL} at different frequencies, such as for example $2\omega_1$, $2\omega_2\ldots$ Here we consider only the terms at ω_1, ω_2 and ω_3 by assuming that only the interaction between these three fields is efficient, due to the phase-matching condition. It is possible then to derive from Eq. 1.71 the following three equations[2] for the fields at ω_1, ω_2 and ω_3:

$$\frac{\partial A_1}{\partial z} + \frac{1}{v_{g1}}\frac{\partial A_1}{\partial t} - \frac{i}{2}k_1''\frac{\partial^2 A_1}{\partial t^2} = -i\frac{\mu_0 \epsilon_0 c_0 \omega_1}{2n_1}d_{eff}A_2^* A_3 exp\left[-i(k_3 - k_2 - k_1)z\right] \tag{1.80}$$

$$\frac{\partial A_2}{\partial z} + \frac{1}{v_{g2}}\frac{\partial A_2}{\partial t} - \frac{i}{2}k_2''\frac{\partial^2 A_2}{\partial t^2} = -i\frac{\mu_0 \epsilon_0 c_0 \omega_2}{2n_2}d_{eff}A_1^* A_3 exp\left[-i(k_3 - k_2 - k_1)z\right] \tag{1.81}$$

$$\frac{\partial A_3}{\partial z} + \frac{1}{v_{g3}}\frac{\partial A_3}{\partial t} - \frac{i}{2}k_3''\frac{\partial^2 A_3}{\partial t^2} = -i\frac{\mu_0\epsilon_0 c_0\omega_3}{2n_3}d_{eff}A_1 A_2 exp\left[-i\left(k_1 + k_2 - k_3\right)z\right]$$

$$(1.82)$$

In the following the "**wave-vector mismatch**" will be defined as: $\Delta k = k_3 - k_1 - k_2$, and the nonlinear interaction coefficient as $d_{eff} = \frac{\chi^{(2)}}{2}$. The three equations are coupled nonlinear partial differential equations, and in general not amenable to an analytic solution and must be treated numerically. A first simplification, that captures the main physics of parametric interaction, consists in neglecting the GVD terms, i.e. putting $k_i'' = 0$. This is justified by considering that the three interacting pulses are propagating at very different group velocities v_{gi}^2. The effects of this group velocity difference are much more relevant than those of group velocity dispersion between the different frequency components of a single pulse. The coupled equations then become:

$$\frac{\partial A_1}{\partial z} + \frac{1}{v_{g1}}\frac{\partial A_1}{\partial t} = -i\kappa_1 A_2^* A_3 exp\left[-i\Delta kz\right]$$

$$(1.83)$$

$$\frac{\partial A_2}{\partial z} + \frac{1}{v_{g2}}\frac{\partial A_2}{\partial t} = -i\kappa_2 A_1^* A_3 exp\left[-i\Delta kz\right]$$

$$(1.84)$$

$$\frac{\partial A_3}{\partial z} + \frac{1}{v_{g3}}\frac{\partial A_3}{\partial t} = -i\kappa_3 A_1 A_2 exp\left[i\Delta kz\right]$$

$$(1.85)$$

with the nonlinear coupling constants defined as: $\kappa_i = \frac{\omega_i d_{eff}}{2c_0 n_i}$. They can be simplified by moving to a frame of reference translating with the group velocity of the pump pulse: $t' = t - \frac{z}{v_{g3}}$. The equations then become:

$$\frac{\partial A_1}{\partial z} + \delta_{13}\frac{\partial A_1}{\partial t} = -i\kappa_1 A_2^* A_3 exp\left[-i\Delta kz\right]$$

$$(1.86)$$

$$\frac{\partial A_2}{\partial z} + \delta_{23}\frac{\partial A_2}{\partial t} = -i\kappa_2 A_1^* A_3 exp\left[-i\Delta kz\right]$$

$$(1.87)$$

$$\frac{\partial A_3}{\partial z} = -i\kappa_3 A_1 A_2 exp\left[i\Delta kz\right]$$

$$(1.88)$$

where $\delta_{i3} = \frac{1}{v_{gi}} - \frac{1}{v_{g3}}$ i=1,2 is the **Group Velocity Mismatch (GVM)**[2] between ω_2/ω_1 and ω_3. These are nonlinear coupled PDEs that can be solved numerically. To get some physical insight, let's start by making the following approximations[2]:

1. Quasi-monochromatic waves, i.e. $\frac{\partial}{\partial t} = 0$

2. Low emptying of the beam at ω_3, i.e. the conversion efficiencies are so low that $A_3 \cong A_{30} = const.$

The coupled equations in this case become:

$$\frac{\partial A_1}{\partial z} = -i\kappa_1 A_{30} A_2^* exp\left[-i\Delta kz\right] \tag{1.89}$$

$$\frac{\partial A_2}{\partial z} = -i\kappa_2 A_{30} A_1^* exp\left[-i\Delta kz\right] \tag{1.90}$$

In the OPA section these coupled equations are solved analytically for both cases of mismatch ($\Delta k \neq 0$) and perfect phase-matching ($\Delta k = 0$).

1.2.3 Phase-Matching

Satisfying the condition $\Delta k = k_p - k_0 = 0$ is known as phase-matching. The traditional method to achieve phase-matching is through the use of the birefringence of a nonlinear crystal such as lithium niobate ($LiNbO_3$), and is commonly referred to as birefringent phase-matching.

Birefringent Phase-matching

For interactions among three waves there are two possible birefringent phase-matching conditions. In Type I phase-matching the two longer wavelengths have the same polarization[3], perpendicular to that of the shorter generated wavelength, such as:

$$\begin{aligned} oo &\rightarrow e \\ ee &\rightarrow o \end{aligned} \tag{1.91}$$

This phase-matching is common in second harmonic generation. Using $\Delta k = k_3 - k_2 - k_1$ and $k_i = \frac{2\pi n(\lambda_i)}{\lambda_i}$ it can be seen that the phasematching condition for Type I SHG is given by[2]:

$$\Delta k = 2\pi \left[\frac{n_{2\omega}^{o(e)}}{\lambda_{2\omega}} - \frac{n_\omega^{e(o)}}{\lambda_\omega} - \frac{n_\omega^{e(o)}}{\lambda_\omega} \right] = 0 \qquad (1.92)$$

This is only possible in materials where $n_{2\omega}^{o(e)} = 2n_\omega^{e(o)}$, a condition that can be met in many crystals but is highly limited by the exact dispersion relation of the material, as shown in Figure 1.3. Fortunately some degree of tunability in the phase-matching condition can be achieved by adjusting the angle of the crystal relative to the propagation direction. Light polarized in the plane containing the optic axis and the direction of propagation will experience an angle-dependent refractive index that varies between n_e and n_o. The correct angle necessary for satisfying Equation 1.92 can be found by adjusting the crystal angle from normal incidence or by cutting the crystal so that the new normal interface becomes the phase-matching angle.

Angle tuning introduces walk-off[2] in the Poynting vector of the generated wave which propagates at an angle to the optic axis. Walk-off reduces the spatial overlap between the interacting waves, lowering efficiency. Another downside to angle tuning is that Δk varies rapidly with angle, constraining the acceptance angle for phase-matching. An alternative to angle tuning is to utilize the temperature dependence of the refractive indices. In many optical crystals the rate of change of refractive index temperature is different for the ordinary and extraordinary indices, allowing for tuning of the birefringence, however the temperatures required to meet the desired phase-matching conditions may be inconvenient.

In Type II phase-matching[3] the two longer wavelength waves have perpendicular polarizations, with the shorter generated wavelength having either polarization, the orientation of which depends on the nonlinear crystal properties.

20
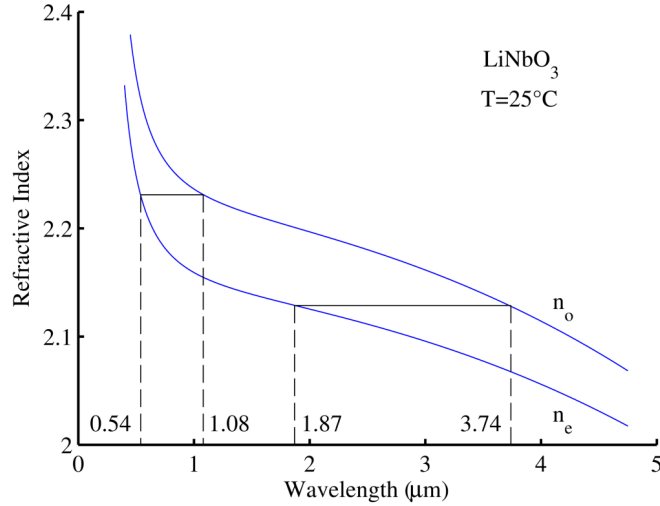
Figure 1.3: Type I birefringent phase-matching solutions for SHG in lithium niobate at $25°C$. The horizontal lines indicate those interactions which simultaneously satisfy the phase-matching and energy conservation conditions of Equation 1.92. Solutions are obtained for SHG of $0.54\mu m$ from $1.08\mu m$ and $1.87\mu m$ from $3.74\mu m$.

Notation is given by:

$$oe \rightarrow e$$
$$oe \rightarrow o$$

(1.93)

Satisfying $\Delta k = 0$ for Type II phase-matching follows the same methodology as for Type I phase-matching, but will not be discussed further here.

Quasi Phase-Matching

An alternative approach to achieving efficient frequency generation in a second-order nonlinear interaction is the case where $\Delta k \neq 0$, known as **quasi phase-matching**[4]. This process takes advantage of the fact that all $\chi^{(2)}$ materials are dispersive. Again considering the case of three interacting electromagnetic waves, the relative phase between them after some propagation distance will accumulate to π, given as:

21

$$\Delta\phi = \phi_3 - \phi_2 - \phi_1 = \pi \tag{1.94}$$

The conversion efficiency builds to a maximum over this propagation distance which is known as the coherence length, given by[2]:

$$L_c = \frac{\pi}{\Delta k} \tag{1.95}$$

After the waves propagate beyond the coherence length the converted intensity decreases as the phase-matching condition has changed. In fact the condition is such that energy is converted from the generated frequencies back into the fundamental frequency, a process known as back conversion. To prevent back conversion and increase the efficiency of the forward conversion, a phase step of π is added to the interacting fields, returning to the phase-matching condition. Physically this phase step is added by periodically flipping the polarity of the nonlinear coefficient tensor $\chi_{ijk}^{(2)}$ by the quasi phase-matching or grating period Λ_g, given by[2]:

$$\Lambda_g = \frac{2\pi}{\Delta k} \tag{1.96}$$

The quasi phase-matching condition is therefore given by:

$$\Delta k_{qpm} = k_3 - k_2 - k_1 - \frac{2\pi}{\Lambda_g} = 0 \tag{1.97}$$

Satisfying this condition can be achieved by varying the length of the grating period, under the condition that:

$$\Lambda_g = \left[\frac{n\left(\lambda_3\right)}{\lambda_3} - \frac{n\left(\lambda_2\right)}{\lambda_2} - \frac{n\left(\lambda_1\right)}{\lambda_1} \right]^{-1} \tag{1.98}$$

Periodic inversion of the nonlinear polarity of a material is achieved through the periodic poling technique. Ferro-electric crystals such as $KTiOPO_4$ are exposed to an intense electric field which alters the position of the ions inside the unit cell[4]. Manufacturers can extend this technique across a crystal by using a patterned electrode to create alternating poled domains with few-micron-scale grating periods over a crystal length of several centimeters. The

QPM process allows for efficient frequency conversion in nonlinear materials where phase-matching is not possible. The relative efficiencies for SHG are shown in Figure 1.4 as an example[2].
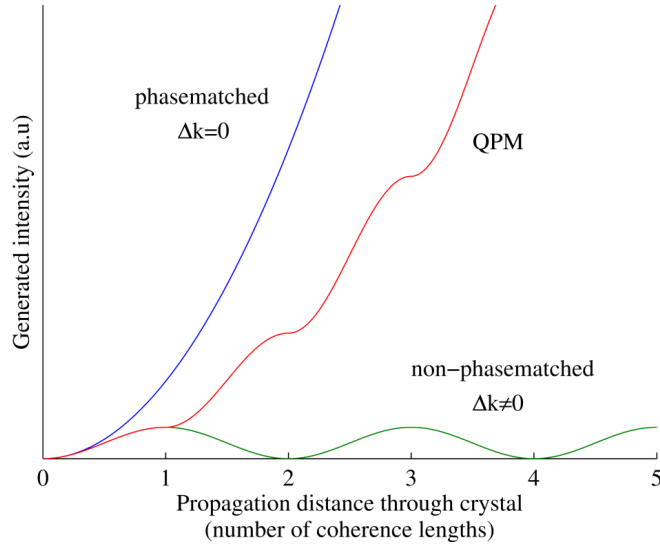
Figure 1.4: Quasi phase-matching allows efficient frequency conversion in non-phase-matched crystals by introducing a π phase shift whenever the phase mismatch accrues to π.

1.3 Optical Parametric Amplifier (OPA)

The Optical Parametric Amplifier (OPA) is a nonlinear device that exploits the amplification of a beam called Signal through the use of a second order nonlinear crystal ($\chi^{(2)}$). Typically there are two beam entering the nonlinear crystal (the Pump beam at ω_p and the Signal at ω_s) and there are three beams exiting the crystal:

- The depleted Pump beam at ω_p

- The amplified Signal beam at ω_s

- The generated Idler beam at $\omega_i = \omega_p - \omega_s$ (DFG)
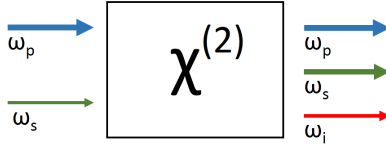
Figure 1.5: OPA schematic of the process. The dimension of the arrows is proportional to the intensities of the beams.

In Figure 1.5 it's reported a simple scheme of the process.

Remembering Equations 1.89 and 1.90, replacing ω_3 with ω_p, ω_2 with ω_s and ω_1 with ω_i, we can start solving the coupled equations for an OPA in the phase-matched and in the mismatched cases (where $\omega_p > \omega_s > \omega_i$).

Perfect Phase-Matching: $\Delta k = 0$

In perfect phase-matching conditions Equations 1.89 and 1.90 become:

$$\frac{dA_1}{dz} = -i\kappa_1 A_{30} A_2^*$$

(1.99)
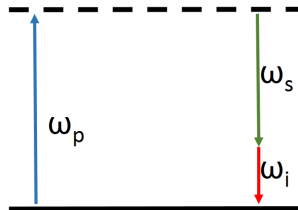
Figure 1.6: Corpuscular representation of the OPA process. The excited level is in dashed lines because is a virtual excited level.

$$\frac{dA_2}{dz} = -i\kappa_2 A_{30} A_1^* \tag{1.100}$$

By taking the derivative of 1.100 with respect to z:

$$\frac{d^2 A_2}{dz^2} = -i\kappa_2 A_{30} \frac{dA_1^*}{dz} = \kappa_1 \kappa_2 |A_{30}|^2 A_2 \tag{1.101}$$

By defining: $\Gamma^2 = \kappa_1 \kappa_2 |A_{30}|^2 = \frac{\omega_1 \omega_2 d_{eff}^2}{4 c_0^2 n_1 n_2} |A_{30}|^2 = \frac{\omega_1 \omega_2 d_{eff}^2}{2 \epsilon_o c_0^3 n_1 n_2 n_3} I_{30}$, we obtain:

$$\frac{d^2 A_2}{dz^2} - \Gamma^2 A_2 = 0 \tag{1.102}$$

The solutions of this equation are:

$$A_2(z) = C_1 exp(\Gamma z) + C_2 exp(-\Gamma z) \tag{1.103}$$

By using the boundary conditions:

$$A_2(0) = A_{20} \tag{1.104}$$

$$A_1(0) = 0 \tag{1.105}$$

which correspond to injecting in the nonlinear crystal a seed at the Signal frequency but not at the Idler frequency, we obtain:

$$A_2(z) = A_{20} \left(\frac{e^{\Gamma z} + e^{-\Gamma z}}{2} \right) = A_{20} cosh(\Gamma z) \tag{1.106}$$

Which, for large values of Γz, becomes:

$$A_2(z) \cong \frac{A_{20}}{2} e^{\Gamma z} \tag{1.107}$$

At the output of a crystal with length L, the amplified Signal intensity becomes:

$$I_2(L) = \frac{I_{20}}{4} e^{2\Gamma L} \tag{1.108}$$

The **parametric gain** is therefore defined as:

$$G = \frac{I_2(L)}{I_{20}} = \frac{1}{4}e^{2\Gamma L} \tag{1.109}$$

The Idler beam amplitude can be easily obtained by integrating 1.99 as[2]:

$$A_1(z) = -i\kappa_1 A_{30} A_{20}^* \frac{sinh(\Gamma z)}{\Gamma} \tag{1.110}$$

and its intensity, in the large gain limit, becomes:

$$A_1(z) = -i\kappa_1 A_{30} A_{20}^* \frac{exp(\Gamma z)}{2\Gamma} \tag{1.111}$$

The idler intensity is then written as:

$$I_1(L) = \frac{\kappa_1}{\kappa_2}\frac{n_1}{n_2}I_2(L) = \frac{\omega_1}{\omega_2}I_2(L) \tag{1.112}$$

Mis-Matching: $\Delta k \neq 0$

In the case of non-vanishing phase mismatch Δk, by taking the derivative of Eq. 1.90 with respect to z we obtain:

$$\frac{d^2 A_2}{dz^2} = -i\kappa_2 A_{30}\left(\frac{dA_1^*}{dz} - i\Delta k A_1^*\right)exp(-i\Delta kz) \tag{1.113}$$

which, with the help of 1.89 and its complex conjugate, can be rewritten as:

$$\frac{d^2 A_2}{dz^2} + i\Delta k\frac{dA_2}{dz} - \Gamma^2 A_2 = 0 \tag{1.114}$$

Eq. 1.114 is a second-order linear differential equation, which has solution of the kind:

$$A_2(z) = e^{\gamma z} \tag{1.115}$$

where γ are the solutions of the corresponding characteristic equation:

$$\gamma^2 + i\Delta k\gamma - \Gamma^2 = 0 \tag{1.116}$$

with the following solutions:

$$\gamma_{1/2} = -i\frac{\Delta k}{2} \pm \sqrt{\Gamma^2 - \left(\frac{\Delta k}{2}\right)^2} = -i\frac{\Delta k}{2} \pm g \qquad (1.117)$$

with $g = \sqrt{\Gamma^2 - \left(\frac{\Delta k}{2}\right)^2}$. A generic solution can be written as:

$$A_2(z) = exp\left(-i\frac{\Delta kz}{2}\right)[C_1 exp(gz) + C_2 exp(-gz)] \qquad (1.118)$$

which, with the boundary conditions $A_2(0) = A_{20}$, $A_1(0) = 0$, become[2]:

$$A_2(z) = A_{20} exp\left(-i\frac{\Delta kz}{2}\right)\left[cosh(gz) + \frac{i\Delta k}{2g} sinh(-gz)\right] \qquad (1.119)$$

The Signal intensity can now be written as:

$$I_2(z) = I_{20}\left[cosh^2(gz) + \frac{\Delta k^2}{4g^2} sinh^2(gz)\right] \qquad (1.120)$$

which, after some manipulation[2], becomes:

$$I_2(z) = I_{20}\left[1 + \frac{\Gamma^2}{g^2} sinh^2(gz)\right] \qquad (1.121)$$

so that the parametric gain can be written as:

$$G(\Delta k, L) = \frac{I_2(L)}{I_{20}} = 1 + \frac{\Gamma^2}{g^2} sinh^2(gL) \qquad (1.122)$$

or, in the large gain case $gL >> 1$:

$$G(\Delta k, L) \cong \frac{\Gamma^2}{4g^2} e^{2gL} \qquad (1.123)$$

We now calculate the wave-vector mismatch that reduces the parametric gain to half:

$$G\left(\Delta k\right) = \frac{G\left(0\right)}{2} = \frac{1}{2}\frac{1}{4}exp\left(2\Gamma L\right)$$
$$\frac{\Gamma^2}{4g^2}exp\left(2gz\right) = \frac{1}{2}\frac{1}{4}exp\left(2\Gamma L\right) \tag{1.124}$$

By neglecting the pre-exponential factor in the gain variation[2], we get:

$$2gL \cong 2\Gamma L - ln2 \tag{1.125}$$

To the first order, g can be expanded as: $g \cong \Gamma - \frac{\Delta k^2}{8\Gamma}$, resulting in:

$$\Delta k = 2\left(ln2\right)^{\frac{1}{2}}\left(\frac{\Gamma}{L}\right)^{\frac{1}{2}} \tag{1.126}$$

In order to calculate the **phase-matching bandwidth** for the OPA process, let us now link the wave-vector mismatch to the frequency variation. Let us assume that the phase-matching condition is rigorously satisfied for a set of frequencies $\bar{\omega_1}, \bar{\omega_2}, \bar{\omega_3}$, with $\bar{\omega_1} + \bar{\omega_2} = \bar{\omega_3}$, so that:

$$k\left(\bar{\omega_1}\right) + k\left(\bar{\omega_2}\right) = k\left(\bar{\omega_3}\right) \tag{1.127}$$

We now keep ω_3 fixed and vary the Signal frequency: $\omega_2 = \bar{\omega_2} + \Delta\omega$. The Idler frequency will consequently vary as: $\omega_1 = \bar{\omega_1} - \Delta\omega$. The wave-vector mismatch will be:

$$\Delta k = k\left(\bar{\omega_3}\right) - \left(k\left(\bar{\omega_2}\right) + \frac{\partial k}{\partial\omega}|_{\bar{\omega_2}}\Delta\omega + \frac{1}{2}\frac{\partial^2 k}{\partial\omega^2}|_{\bar{\omega_2}}\Delta\omega^2 + ...\right) -$$
$$\left(k\left(\bar{\omega_1}\right) + \frac{\partial k}{\partial\omega}|_{\bar{\omega_1}}\left(-\Delta\omega\right) + \frac{1}{2}\frac{\partial^2 k}{\partial\omega^2}|_{\bar{\omega_1}}\left(-\Delta\omega\right)^2 + ...\right) \tag{1.128}$$

In 1.128 we have stopped the wave-vector expansion to the second order. Taking into account 1.127, Eq. 1.128 can be rewritten as:

$$\Delta k \cong -\left(\frac{1}{v_{g2}} - \frac{1}{v_{g1}}\right)\Delta\omega - \frac{1}{2}\left(k_1'' + k_2''\right)\Delta\omega^2 \tag{1.129}$$

This shows that, to the first order, the wave-vector mismatch is proportional to the GVM between Signal and Idler pulses: $\delta_{12} = \frac{1}{v_{g1}} - \frac{1}{v_{g2}}$, $\Delta k \cong \delta_{12} \Delta \omega$. The FWHM gain bandwidth, using 1.126, can then be written as:

$$\Delta \nu_{FWHM} = \frac{2 \left(ln \left(2\right)\right)^{\frac{1}{2}}}{\pi} \left(\frac{\Gamma}{L}\right)^{\frac{1}{2}} \frac{1}{|\delta_{12}|} \tag{1.130}$$

Eq. 1.130 shows that, in order to achieve a broad phase matching bandwidth, the group velocities of Signal and Idler frequencies should be matched (**group-velocity matched OPA**). In the case of $\delta_{12} = 0$, the wave-vector mismatch must be expanded to the second order in $\Delta \omega$, giving:

$$\Delta \nu_{FWHM} = \frac{\sqrt{2} \left(ln \left(2\right)\right)^{\frac{1}{4}}}{\pi} \left(\frac{\Gamma}{L}\right)^{\frac{1}{4}} \frac{1}{|k_1'' + k_2''|^{\frac{1}{2}}} \tag{1.131}$$

and is thus inversely proportional to the sum of the GVDs of Signal and Idler pulses. In both cases the gain bandwidth increases with increasing non-linearity Γ and decreases for increasing crystal length L, but the dependence is quite weak.

In order to achieve broadband phase matching, it is therefore necessary to have $\delta_{12} = 0$, i.e. to achieve **group velocity matching between Signal and Idler pulses**.

1.4   Optical Parametric Oscillator (OPO)

1.4.1   Introduction

The results reported in the previous section indicate that amplification via the $\chi^{(2)}$ non-linearity is possible. Here is achieved through the implementation of a resonant cavity known as an optical parametric oscillator (OPO) that enhances the parametric optical amplification, illustrated in Figure 1.7. The three frequencies of the three interacting waves $\omega_3 > \omega_2 \geq \omega_1$ are denoted as the Pump ω_p, Signal ω_s and Idler ω_i respectively. When the cavity mirrors are coated such that they are highly reflective at the Signal or Idler frequency then the cavity is said to be singly-resonant[1]. If the high reflectivity regions

extend to both the Signal and Idler waves then the cavity is said to be doubly-resonant. For the special case where the resonant Signal and Idler frequencies overlap at half the Pump frequency, the OPO is said to be degenerate[5].
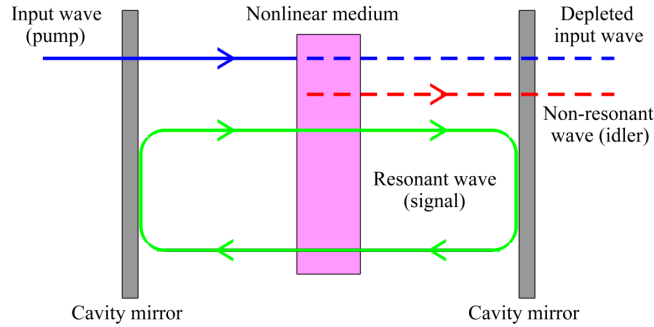

Figure 1.7: A simple illustration of a singly-resonant optical parametric oscillator. The Pump wave is coupled into the nonlinear medium through a dichroic cavity mirror. The Pump wave is converted into a non-resonant Idler wave and a resonant Signal wave. The Signal wave can be coupled out of the resonator with a standard partially-reflective cavity mirror.

As with the case of OPA, both the Signal and Idler waves increase in intensity as they propagate through the nonlinear crystal. All the equations of the OPA describe the OPO in terms of a single "round-trip" in the cavity (one pass through the crystal). The OPO is an optical cavity and, after many round-trips (many passes through the crystal), the Signal that we encounter has a narrower band-width and a different intensity (is a balance between the gain of the crystal and the losses in the cavity) from the one given by the OPA's solutions[6]. The main difference between OPAs and OPOs is that the last one is not seeded, there isn't an external Signal to be amplified; in fact during the first round-trip of the cavity the Signal is generated by the process of OPG (Optical Parametric Generation), then each round-trip can be describe by the process of OPA.

Optical parametric oscillators are widely used as highly tunable sources, limited by the phase-matching conditions of the nonlinear crystal and the reflective coating of the resonator mirrors. OPOs can be operated both intra-and extra-cavity, in CW-mode or in a pulsed regime, with pulse durations

ranging from nanoseconds to femtoseconds[1]; all depending on the phase-matching conditions and cavity geometry.

An extra requirement must be satisfied for pulsed operation. The OPO must be synchronously pumped[7], so that the cavity length of the OPO matches the repetition rate of the Pump laser. This requirement arises due to the lack of absorption and gain storage in an OPO; the nonlinear gain process is instantaneous and so the generated electric fields only build up if a generated pulse coherently overlaps after one round-trip with the next incident Pump pulse inside the crystal.

1.4.2 A Brief Historical Review

The field of nonlinear optics has developed rapidly since the demonstration of second harmonic generation in 1961: this experimental demonstration of nonlinear interaction between intense optical fields and medium has started the expanding field of nonlinear optics. The progress in this field since 1961 has been described in many reviews and articles[8].

In 1965 Wang and Racette[8] observed significant parametric gain and in the same year was demonstrated the first Optical Parametric Oscillator (OPO) using $LiNbO_3$. The success of the first OPO pushed towards finding new nonlinear materials; in fact in 1966 was demonstrated the oscillation for an OPO using a KDP (KH_2PO_4) crystal[8]. The following OPOs were mostly pumped by high peak power pulsed lasers utilizing as nonlinear crystal $LiNbO_3$ or KDP. The tuning range of these devices increased rapidly from IR region to the visible region.

Nowadays such optical parametric devices have become sufficiently reliable for routine and trouble-free operation[1]. Some 15 years ago Ti:sapphire and dye lasers were joined by these nonlinear optical devices because of their tuning range that is now extended in the ultraviolet, visible, near-infrared and mid-infrared, and for the solid state character and high efficiency[1]. The wide tuning range of OPOs has opened up prospects for laser spectroscopy in otherwise inaccessible spectral regions.

With the coming of the Quasi Phase-Matching (QPM) Technique the ex-

ploiting of big nonlinear optical gain enhancement, relative to its Birifrangent Phase-Matching (BPM) counterpart, has revolutionized the design of optical parametric wavelength-conversion devices (such as OPG, OPA, OPO and DFG). The discovery of QPM materials such as PPLN (periodically poled lithium niobate) have been widely reported recently, making these materials the most versatile nonlinear crystal present at the moment. This versatility is due to the poling process, which produces a periodic modulation, or grating, that can be chosen to provide phase-matching of any frequency conversion process such that the crystal properties can be precisely tailored to the requirements of the user[9].

In contrast to BPM, QPM allows a combination of propagation direction and polarizations to be selected that exploit the largest nonlinear coefficient of the crystal. A further useful consequence of this arrangement is that all waves propagate collinearly along a crystal axis, thus avoiding the drawbacks of Poynting vector walk-off and the difficulties inherent in attempting to compensate for it, such as the use of noncollinear phase-matching.

Summarizing all these differences between OPOs and Lasers[10,1]:

- Whereas many lasers can be operated with spatially incoherent pump sources, a parametric oscillator requires relatively high spatial coherence of its pump. In most cases, a diode-pumped solid-state laser is used.

- No heat is deposited in the nonlinear crystal, unless there is some parasitic absorption at the pump, signal or idler wavelength. As OPOs are mostly operated with all wavelengths involved lying well within the transparency region, there is normally not much heating. Only at fairly high power levels may a disturbance of the phase-matching conditions occur. Thermal lensing is usually not significant.

- Whereas the emission wavelength of most lasers can be tuned only in a narrow range, many parametric oscillators offer the potential for wavelength tuning with extremely wide tuning ranges. These may span regions in the visible, near or mid-infrared part of the electromagnetic spectrum.

- The parametric amplification process requires phase matching to be efficient. The phase-matching details also determine the oscillation wavelength. Wavelength tuning is in most cases achieved by influencing the phase-matching conditions, e.g. by changing the crystal temperature, the angular orientation of the crystal (for critical phase matching), or the poling period (for quasi-phase matching in periodically poled crystals). Within the phase-matching bandwidth, tuning is also possible with an intracavity optical filter. The tuning range can be limited either by restrictions of phase matching, or by the transparency region of the nonlinear material or by the spectral region with high reflectivity of the resonator mirrors.

- The parametric amplification occurs only in the direction of the pump beam (as another consequence of phase matching), which means that a unidirectional operation in a ring resonator is automatically obtained.

- No energy is stored in the nonlinear crystal. Therefore, the gain is present only as long as the pump wave is there, and pump fluctuations directly affect the signal power. The dynamics are therefore different to laser dynamics.

- Other than the fluorescence of a laser gain medium, parametric fluorescence occurs only in the direction of the pump beam. More precisely, it is observed in those modes which experience parametric gain.

- An idler wave is generated, which carries away the difference between the generated signal power and the absorbed pump power. (Only in the rarely used case of degenerate parametric oscillation, is there no idler wave.) More precisely, the photon energy of the idler wave is the difference in the photon energies of the pump and signal. The idler wave plays an essential role in the nonlinear conversion process; when an OPO is operated in a spectral region with strong idler absorption in the crystal, the threshold pump power can be much higher, and the efficiency lower.

- Phase coherence between Signal, Idler and Pump is essential.

Now let's analyze OPOs marking the different operating regimes in four classes, each one referred to a single-pass optical parametric gain process. This classification was reported in *Solid-State Mid-Infrared Sources* of Ebrahimzadeh, M., Berlin, 2003.

	Class A continuous-wave	Class B ns-pulsed	Class C modelocked	Class D modelocked and amplified
Pump pulse energy		10 mJ	15 nJ	10 μJ
Pump pulse duration		10 ns	100 fs	200 fs
Peak pump intensity I_p	0,4 MWcm^{-2}	30 MWcm^{-2}	20 GWcm^{-2}	7 TWcm^{-2}
Crystal length L	10 mm	10 mm	1 mm	1 mm
ΓL ($\equiv$gL if Δk=0)	0,09	0,77	1,99	37
G_I(L)	0,008	0,72	13	3,4 x 10^{31}
Optical parametric devices	OPO	OPO	OPO	OPO, OPG, OPA

Table 1.1: Typical Operating Regimes for Different Classes (A-D) of Single-Pass Optical Parametric Gain Process[1]

The table is based on typical experimental values for pump laser and NLO material parameters in each operating regime. The parametric gain factor ΓL and single-pass power G_I(L) are calculated on the basis of near-degenerate operation with $\lambda_S \approx \lambda_I \approx 2\mu m$. Typical NLO material parameters are

assumed, and the four operating regimes are distinguished by choice of pump power, focal geometry, crystal length L, and (for cases B-D) pump pulse duration. The resulting values of $G_I(L)$ range over 33 orders of magnitude, from low power CW operation (A) to high-energy ultrafast pulsed operation (D). Usually, the signal and idler output power from an optical parametric device must build up from spontaneous parametric emission, so that only the high-energy ultrafast pulsed case (D) has sufficiently high single-pass power gain $G_I(L)$ to enable practical operation as an OPG or an OPA, as in Table 1.1 respectively. In such a situation, the parametric gain in the other three operating regimes (CW, Q-switched, and modelocked; cases A, B, and C, respectively) is typically too small to build up to a significant output power from spontaneous parametric emission. It is then necessary to adopt the OPO strategy, with the NLO medium enclosed in an optical cavity to provide resonant optical feedback at the signal/idler wavelengths.

Chapter 2

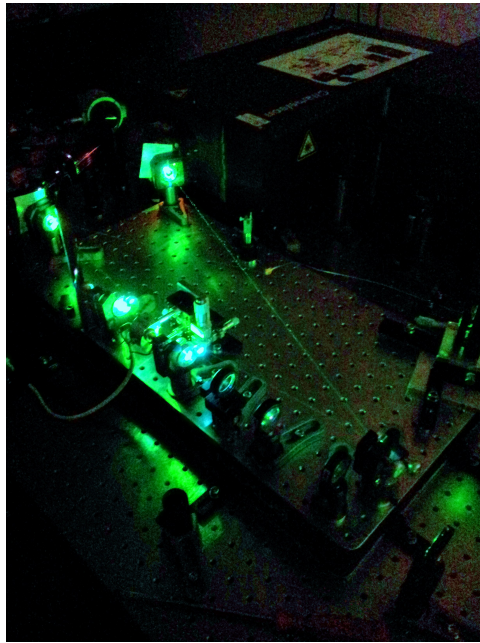# Design of a Synchronously Pumped Ultrafast OPO

Figure 2.1: OPO cavity photo during operation. The green light in the cavity is the second harmonic of the Signal at 1100 nm.

2.1 Introduction

In this chapter the experimental part that truly covered this thesis is going to be described. The purpose of this thesis was the construction of a light source for a TRPL (Time Resolved Photo-Luminescence) lab in the Center for Nanoscience and Technology (CNST) at the Italian Institute of Technology (IIT). In this lab there was already a light source, a Ti:sapphire Chameleon II Ultra made by Coherent that emits $150fs$ pulses with $80MHz$ of repetition-rate at $780nm$ (the repetition-rate can vary from $\pm700KHz$ changing the wavelength) tunable from $680nm$ to $1080nm$. Using the second harmonic of the fundamental is possible to cover the range from $340nm$ to $540nm$, leaving to discover the range from $540nm$ to $700nm$.

The idea was to build up a source with the following specifics:

1. An output tunable from $540nm$ to $700nm$

2. Generating pulses of $2ps$ duration, to the maximum, at $80Mhz$ of Repetition Rate

3. Easy to use

4. Not expensive

5. Enough stable (in terms of spectrum and power) to make TRPL measurements

For these reasons an OPO was chosen; in fact Optical Parametric Oscillators are versatile, easily tunable, stable and coherent sources.

It was chosen to pump the OPO with $780nm$ (where the $RR = 80MHz$) and to generate an output between $1000nm$ and $1400nm$, doubling this output it was possible to obtain the desired range. Because the Pump is an ultra-fast source the OPO must be synchronous with the repetition-rate of the Pump laser in order to achieve oscillation inside the cavity: it is an OPO of Class C, as we can see in the Table 1.1. Getting about the temporal requirements of the output pulses coming from the OPO, is important to know the temporal limitations in terms of resolution introduced by the acquisition

system during a measurement. In this lab the acquisition system has $2ps$ of estimated temporal resolution and works at a repetition-rate of 80 MHz. So the output pulses coming from the OPO would have to be at maximum of $2ps$ duration and at $80MHz$. Without strict temporal requests it was decided to build up an OPO with no temporal compression inside/outside the cavity and with a long non-linear crystal.

In the next chapter the OPO design choices made in order to obtain the requirements mentioned before will be described.

It's important to mention that this OPO was built in collaboration with a Scottish Phd Student expert in OPOs, Richard McCracken, that hosted me in his university (Heriot-Watt University) in order to gain experience in the design and in the implementation of OPOs.

2.2   OPO's Typical Layout

Making a simple scheme of an OPO, this is what we obtain, as the Figure below shows.

Figure 2.2: OPO scheme.

Entering the OPO cavity there's only the Pump beam, obtaining as output three beams: the Signal, the residual Pump and the Idler. In order to obtain the desired output there must be chosen the right properties of the cavity: type of crystal, Pump wavelength and cavity design.

Summarizing all the decisions to be taken in order to build the specific OPO for the desired application, these are the fundamental constituent parts of the general layout of an OPO:

- *Input and Conditioning*: choice of the Pump wavelength and of the optical elements before entering the cavity, in order to obtain the right

38

Pump beam properties to exploit the non-linear phenomenon (right focusing of the Pump on the crystal, isolators, half-wave plates, etc...).

- *Cavity*: choice of the cavity design (ring cavity or linear cavity) and of the opto-mechanical parts present in the cavity (mirror mounts and crystal mount, mirrors' curvature), choice of the range of reflectance of the cavity mirrors (singly resonant cavity or doubly resonant cavity), choice of the type of phase-matching and of the crystal type.

- *Output*: choice of the Signal wavelength (the output of the cavity) and of the Output Coupler (OC).

After having fixed the Pump wavelength and the central Signal wavelength, the choice of the cavity parameters and of the crystal are strictly correlated. In fact the type of PM (phase-matching) will influence the bandwidth of the Signal (Output) and also the choice of the range of reflectance of the cavity mirrors, in order to make the Signal resonant in the cavity. Another important parameter is the OC: the higher are OC losses, the higher will be the threshold power of the cavity and the output power.

The importance of the input stage before entering the cavity is crucial: if the Pump beam is not rightly focused in the crystal there will be a low conversion efficiency in the non-linear phenomenon and so the threshold power of the cavity will be increased. If the Pump beam polarization is not parallel to the right axis of the crystal the Signal won't experience a sufficiently high gain in order to overcome the cavity losses.

In Figure 2.3 it is shown a typical layout of an OPO linear cavity, which contains two plano-concave mirrors for focusing the Signal on the crystal, one plane end mirror, one OC and the crystal. The OC and one of the two plano-concave mirrors are positioned on a translator stage in order to control the stability parameters of the cavity itself. The translation stage on the OC serves to control the cavity length for matching the RR (repetition rate) of the Pump, in the case of a synchronously pumped OPO. The translation stage on the plano-concave mirror serves to control the Signal divergence after the crystal: the distance between this mirror and the crystal is crucial
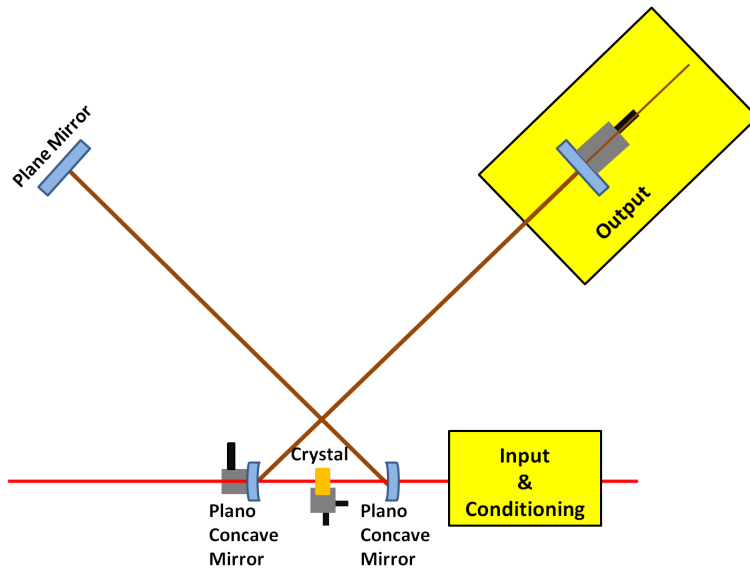
Figure 2.3: OPO general layout. In red is represented the Pump beam and in brown the Signal beam.

for the cavity stability.

In the next section the choices made about the three constituent parts of a general OPO layout will be described, in order to built one with the specifics mentioned in the Introduction section of this chapter.

2.3 Design

The design of an ultrafast OPO has three main stages. First the wavelength outputs must be chosen for the purpose of the experiment. The potential wavelength outputs will be constrained by the Pump wavelength, by the phase-matching properties of the nonlinear crystal and by the wavelength limitations introduced by the acquisition system parameters. The choice of the crystal material will depend on the desired center wavelength and bandwidth(s) of the resonant pulse(s), as well as the type of phase-matching employed. The thickness of the crystal will impact the gain of the Signal/Idler pulses and will also affect the intra-cavity dispersion of the OPO. Finally

the opto-mechanical design of the cavity will play an important role in the stability and efficiency of the parametric process. Each of these stages must be considered when designing and constructing an OPO.

Now all the different aspects of the OPO will be considered in detail.

2.3.1 Pump and Signal

For a given Pump wavelength there is a finite number of Signal and Idler wavelengths that can be generated in a parametric process. The sum of the Signal and Idler frequencies must always equal the Pump frequency, such that:

$$\omega_p = \omega_s + \omega_i \tag{2.1}$$

or

$$\frac{1}{\lambda_p} = \frac{1}{\lambda_s} + \frac{1}{\lambda_i} \tag{2.2}$$

This allows the possible Signal and Idler wavelengths to be determined for a particular Pump wavelength. Taking into account this, let's consider the specifics that have been listed in the Introduction section of this chapter:

- The Pump is a Ti:sapphire laser generating $150fs$ pulses tunable between $680nm$ and $1080nm$, with maximum average power of $4W$ and with a $RR = 80MHz \pm 700KHz$ changing the wavelength. At $780nm$ the nominal repetition rate is $80MHz$.

- The OPO output must be at $80MHz$ because at $780nm$ the Pump source has the maximum output power, around $4W$.

- The Signal must be continuously tunable from $1000nm$ to $1400nm$ (Idler from $1761nm$ to $3545nm$), with enough power to guarantee tens of milliwatts of its second harmonic ($500nm$ - $700nm$). In fact the aim of this OPO is to generate a visible output for TRPL measurements.

The choices that have been taken about Signal and Pump are the following:

41

1. Fix the Pump at $780nm$ where the repetition rate is exactly $80MHz$ and the output power is the highest that the source can give.

2. Obtain the tuning of the Signal output working on cavity parameters and crystal parameters.

Now, having set the output and the input, is important to guarantee this relationship between them. In the next subsection the choice of the non-linear crystal and the consequent type of phase-matching will be discussed.

2.3.2 Crystal

Once a Signal wavelength range has been selected, the next step is to select a non-linear crystal that will allow efficient Signal generation over that range. The aim is to produce broadband visible outputs, the resonant Signals must also be broadband. The phase-matching possibilities, as efficient Type I or Type II birefringent phase-matching, will be limited by the bandwidth of the pulses. A common solution is to use Type-0 quasi phase-matching[11] (QPM) in order to increase the phase-matching bandwidth without sacrificing gain. The two common periodically-poled nonlinear crystals used for parametric generation from a Ti:sapphire laser are lithium niobate (LiNbO$_3$, PPLN) and potassium titanyl phosphate (KTiOPO$_4$, PPKTP). Table 2.1 lists relevant material properties of both crystals[12,13].

The transmission range of both crystals is sufficiently broad to allow generation of both the resonant Signal wavelengths in the near-IR. The d$_{33}$ coefficient of PPLN is almost double that of PPKTP; gain is proportional to $\frac{d_{33}}{n^3}$ and PPLN provides more gain.

PPLN produces significantly more second-order dispersion in the near-IR and visible than PPKTP, and also requires heating to work effectively as PPLN easily suffers from the photo-refractive effect[14,15]. The photo-refractive effect is caused by coherent beams of light illuminating a material to produce an interference pattern of dark and light fringes. Electrons within the light fringes are excited into the conduction band of the material, where they flow towards the dark fringes. This leaves electron holes in the light fringes,

creating an electric field that in turn causes a change in the refractive index of the material in regions where the field is strongest. A refractive index grating is formed that follows the pattern of the interference fringes, causing the incident light to diffract. Ferroelectrics[16] such as Lithium Niobate, is known to suffer severely from photo-refractive damage, particularly at visible wavelengths.

It was demonstrated experimentally that the Photo-refractive effects in Lithium Niobate can be alleviated[15] by heating the crystal[9], doping with MgO, making the crystal more stoichiometric and making a periodic poling of the crystal (PPLN)[15]; PPKTP is much less susceptible to photo-refractive effects because of its high ionic conductivity which screen any generated bulk field, and so it can operate at room temperature[17].

	PPLN	**PPKTP**
Transmission Range (μm)	0.33 - 5.50	0.35 - 4.50
d$_{33}$ coefficient $\left(\frac{pm}{V}\right)$	25.0	13.7
GDD at 0.8 μm $\left(\frac{fs^2}{mm}\right)$	478.8 (o) 383.1 (e)	151.6
GDD at 1.1 μm $\left(\frac{fs^2}{mm}\right)$	74.5 (o) 58.5 (e)	22.1
Requires heating?	Y	N

Table 2.1: Material properties of PPLN and PPKTP.

The temporal duration of the pulses (about ps pulses) shall not limit the length of the crystal, so it was decided to use a long non-linear crystal[18] of 5 mm. This solution supports higher gain at the expense of bandwidth as Eq. 1.130 and Eq. 1.123 shows. A longer crystal will have an increased gain and produce more intracavity Signal power, however the group delay walk-off between the Pump, Signal and Idler will increase leading to less efficient frequency mixing. The choice of making external doubling of the Signal is also due to this fact: the frequency mixing inside the cavity are less efficient with long crystals, so it was decided to have more Signal power inside the

cavity and doubling it outside the cavity.

It was chosen the PPLN crystal for two reasons:

- Good confirmations of the use of PPLN crystals in near-IR OPOs are reported in many reviews and articles[9,18,19,20].

- Taking the relative number of grating domains and the relative d_{33} coefficients of each crystal into account, a rough calculation[11] suggests an 8:3 signal gain ratio in favor of PPLN.

In order to find the right grating periods Λ_g of the crystal that would phase-match in the range desired for this thesis, a Matlab code was done for the calculations. The equations involved in the calculations were:

$$\frac{1}{\Lambda_g} = \frac{n_p}{\lambda_p} - \frac{n_s}{\lambda_s} - \frac{n_i}{\lambda_i} \tag{2.3}$$

and Equation 2.2.

In these equations λ_p, λ_s, λ_i are respectively Pump, Signal and Idler wavelengths; with the same subscript are written the refractive indices. With these two equations it was possible to find the grating periods of the PPLN that could phase-match the desired Signal range ($1000nm$ - $1400nm$) around $780nm$ Pump.
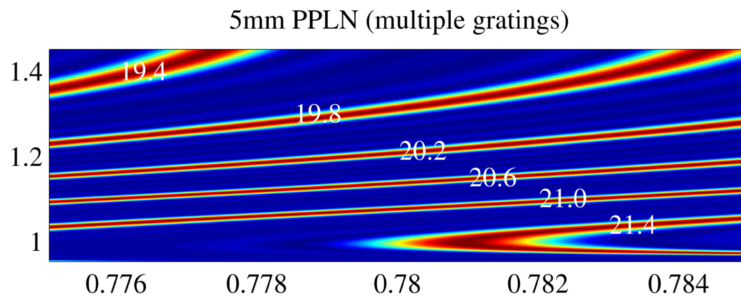

Figure 2.4: $5mm$ PPLN at $80°C$ resulting gratings from the Matlab code. On the x axis there are the Pump wavelengths and on the y axis the Signal wavelengths. Each line in the figure is referred to a different grating whose period is written beside.

After the optimal grating periods for matching the output were found, a search for PPLN crystals in stock with similar grating periods was carried out. It was purchased the PPLN crystal from Covesion (Covesion, United Kingdom), finding one just in stock with the following nine grating periods: 18.50-20.90 μm in 0.30 μm steps. The phase-matching curve is reported below for a crystal temperature of $110°C$. As you can see with this solution it is possible to phase-match all the output range, just by increasing the temperature from the situation in Figure 2.4.
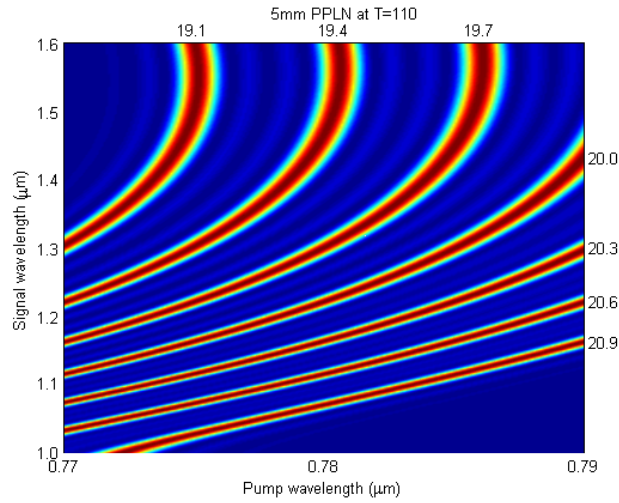

Figure 2.5: Phase-Matching curves for a multiple grating 5 mm long PPLN crystal at 110 degrees.

Figure 2.5 shows that three gratings cannot phase-match with 780 nm (18.5 μm, 18.8 μm, 19.1 μm). In order to use the 19.1 μm grating is necessary a temperature tuning; in fact at $180°C$ this is what happens, as Figure 2.6 reports.
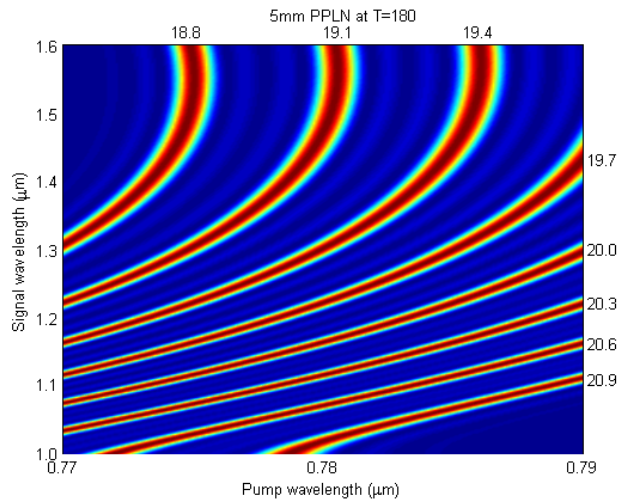
Figure 2.6: Phase-Matching curves for a multiple grating 5 mm long PPLN crystal at 180 degrees.

The design of the PPLN crystal that was used is shown in Figure 2.7. The crystal was grown as a multi-grating, allowing the Signal wavelength to be tuned by moving the crystal in the vertical direction (Y axis), the Signal beam is propagating in the X direction (5 mm). Another important requirement of the crystal is the AntiReflection coating on both its facets at 780 nm and from 1000 nm to 1500 nm, in order to avoid losses caused by reflection at the interfaces.
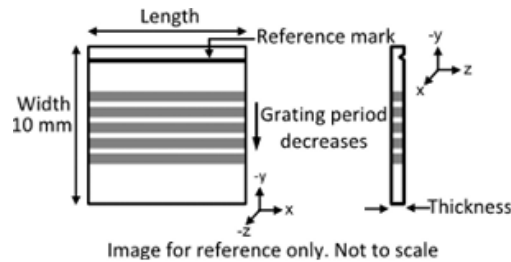

Figure 2.7: PPLN crystal design.

2.3.3 Cavity

In this subsection the design calculations that have been made for the cavity project will be described.

The OPO cavity can be divided in two main parts: the input stage and the resonator. It's important to start with the resonator design in order to obtain the parameters that will serve us to design the right input stage for the cavity.

Resonator

The OPO was designed as a linear "X" resonator (two curved mirrors of radius R1 and two end mirrors), as the Figure below shows.
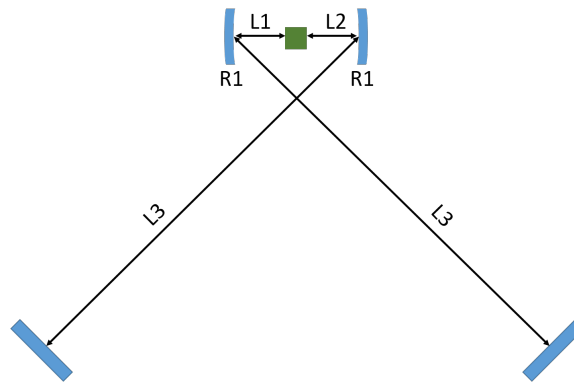

Figure 2.8: OPO cavity resonator in X linear configuration. In green is represented the non-linear crystal.

Figure 2.8 reports the following resonator's parameters:

- The distance L1 and L2 between the curved mirrors and the input/output facet of the crystal

- The mirrors' curvature R1

- The distance L3 between the curved mirrors and the end plane mirrors

The first step in designing a resonator for a synchronously pumped OPO is to set the cavity length. In fact the OPO resonator length must be equal to

the Pump Laser cavity length. Knowing the Pump repetition rate ($80MHz$) it is possible to evaluate the right cavity length for the OPO:

$$L_{cavity} = \frac{c}{2RR} \tag{2.4}$$

and we obtain: $L_{cavity} = 1873.7mm$. It's important to remember that, at the end of the oscillator stability calculations, $L1 + L2 + L3 + L3 + L_{crystal}n\,(\lambda_{Signal}) = L_{cavity}$.

The second step consists in choosing the radius of curvature of the two curved mirrors, this choice will influence the resonant Signal spot dimension inside the crystal. Because the crystal we've chosen is a long one, $5mm$ long, it is important to have a Signal spot with a Rayleigh Range comparable with the length of the crystal itself: in this way the Signal is generated in the cavity for the whole length of the crystal. Excluding short focal lengths that won't guarantee enough long Rayleigh Ranges, a good compromise was R1=$100mm$ (assuming a Signal spot of 1mm before the curved mirror and $n\,(\lambda_{Signal}) = 2.2$, $z_R = \frac{\pi w^2 n}{\lambda} = 2.1mm$).

The third step is to calcuate with the help of a Matlab code the resonator stability, finding the right lengths L1 and L2 that guarantee a stable cavity. The theoretical foundations for the Matlab calculations consist in ABCD matrix theory for stable resonators[21] and Gaussian beams.

From the theory, a general resonator can be described with the matrix formalism as Figure below shows.
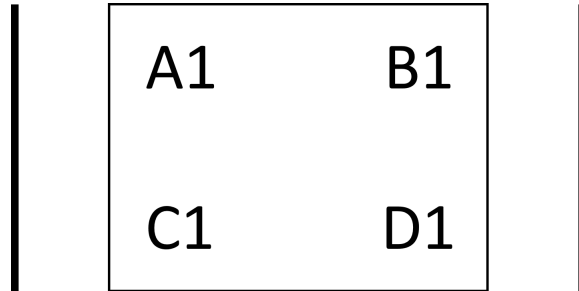

Figure 2.9: ABCD matrix representation of a resonator.

In Figure 2.9 $M1 = \left(\begin{smallmatrix} A1 & B1 \\ C1 & D1 \end{smallmatrix}\right)$ is the matrix describing the propagation

in the resonator from the left plane mirror to the right plane mirror. The stability of the resonator can be described by its round-trip matrix (M_{rt}), that is the resulting matrix from the product of matrix $M1$ with the matrix describing the coming back from the right mirror to the left mirror. It can be shown that the coming back matrix, describing the ray propagation in the resonator from the right mirror to the left mirror, is equal to[21]:

$$M2 = \begin{bmatrix} D1 & B1 \\ C1 & A1 \end{bmatrix} \tag{2.5}$$

and so we can calculate the round-trip matrix as follows:

$$M_{rt} = \begin{bmatrix} D1 & B1 \\ C1 & A1 \end{bmatrix} \begin{bmatrix} A1 & B1 \\ C1 & D1 \end{bmatrix} = \begin{bmatrix} 2A1D1 - 1 & 2B1D1 \\ 2A1C1 & 2A1D1 - 1 \end{bmatrix} = \begin{bmatrix} A & B \\ C & D \end{bmatrix} \tag{2.6}$$

After having calculated this matrix, it is possible to apply the Stability Criterion for a resonator. A resonator is stable if for its round-trip matrix $M_{rt} = \begin{pmatrix} A & B \\ C & D \end{pmatrix}$ applies[21]:

$$-1 < \left(\frac{A+D}{2} \right) < 1 \tag{2.7}$$

Solving this inequality it's possible to find the stability region in which the resonator is stable. Generally the stability region is a function of a parameter, usually the distance between the two curved mirrors of a resonator. The utility of the stability graph is to find the right distances between the optical elements in the resonator.

One single-trip in the resonator in Figure 2.8 can be represented by the sequence of the optical elements in Figure 2.10: where in green is represented the $5mm$ long PPLN crystal and the lenses represent the curved mirrors (in fact $f = \frac{R1}{2}$). The distances shown in Figure 2.10 are set at the right lengths given by the stability graph. In practice all the distances L1, L2 and L3 were set to an initial value that would respect $L_{cavity} = L1 + L2 + L3 + L3 + L_{crystal} n\left(\lambda_{Signal}\right) = 1873.7$. Then these values were cycled in the stability
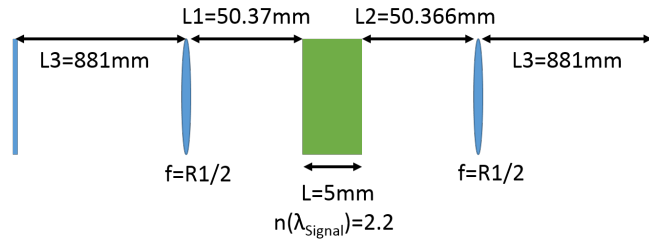
Figure 2.10: Optical elements representation of the single-trip.

program using, as a parameter, the distance L2. From the stability graph it was possible to evaluate the optimal distance L2' (is the value in the middle of the stability region), having fixed all the others. The value L2' given by the program was then set in this way: L2 must be approximately equal to L1 (is a symmetric resonator), so the new values of L2 (L2") and of L1 (L1") will be $L1'' = L2'' = L2 + \frac{L2'-L2}{2}$. Taking into account to change L3 in order to obtain always the same RR. The program was cycled following these steps, until L2" was equal to the optimal L2' given by the program. In the Figure below the stability graph for this resonator is shown.
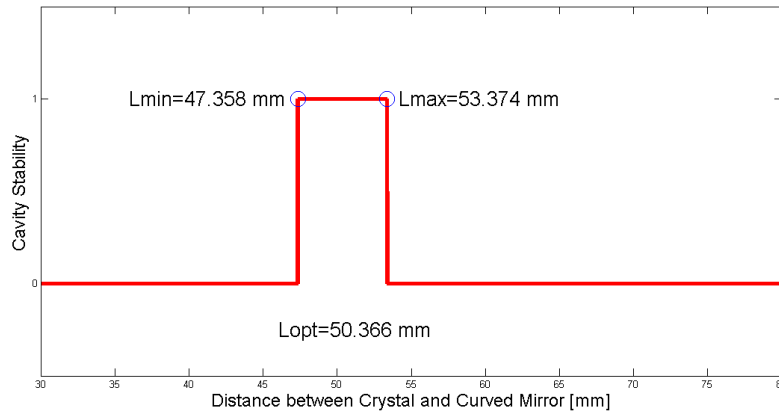

Figure 2.11: Stability Graph of the OPO resonator.

The stability graph reports that the stability region extends from L2$_{min}\cong$47.4mm to L2$_{max}\cong$53.4mm, with fixed L1=50.37mm. The optimal distance L2 is in

the middle of this range: $L2_{opt} \cong 50.37$mm. With this values it is possible to calculate the RR of the cavity, which appears to be:

$$L_{cavity} = L1 + L2 + L3 + L3 + L_{crystal}n\left(\lambda_{Signal}\right) = 1873.736mm$$

which corresponds to a RR of $79.999MHz$ (Eq. 2.4).

The fourth step, having now fixed the resonator parameters, it is to calculate the beam radius of the Signal inside the resonator. The theory behind this is the ABCD matrix theory in approximation of perfectly Gaussian beams[21]. We are interested in the complex beam parameter of a Gaussian beam q:

$$\frac{1}{q} = \frac{1}{R} - i\frac{\lambda}{\pi w^2} \tag{2.8}$$

where R is the radius of curvature of the equiphase surface of the Gaussian beam and w is the beam radius at $1/e^2$ of the maximum intensity (also called beam spot size). It is possible to describe the propagation of a Gaussian beam with the ABCD propagation matrix in the following way[21], through its complex parameter q:

$$q_2 = \frac{Aq_1 + B}{Cq_1 + D} \tag{2.9}$$

where q_2 is the complex parameter after the propagation of q_1 through the ABCD matrix. We are interested in the beam spot $w(z)$ inside the resonator, in order to calculate it at a given point z you have to equal the imaginary parts of Eq. 2.8 and Eq. 2.9. In this way we obtain:

$$w\left(z\right) = \sqrt{-\frac{\lambda}{\pi}\frac{1}{Im\left(\frac{1}{q(z)}\right)}} \tag{2.10}$$

Just by replacing in Eq. 2.9 the ABCD elements relative to a specified distance of propagation $\bar{z}$ inside the resonator we obtain, through Eq. 2.10, the corresponding value of $w(\bar{z})$. It's important to set a starting plane from which to calculate the beam radius in the resonator. It was chosen one of the

two plane mirrors, where the starting complex parameter q_i was calculated from the round-trip matrix shown above, just by imposing the cyclicality on the q parameter itself:

$$q_i = \frac{Aq_i + B}{Cq_i + D} \tag{2.11}$$

obtaining, remembering that from Eq. 2.6 element A is equal to D in the M_{rt}:

$$q_i = i\sqrt{-\frac{B1D1}{A1C1}} \tag{2.12}$$

which is purely imaginary (plane wavefront). From the value of q_i it's possible to calculate the starting beam radius w_i and the spot behaviour inside the resonator (the spot was calculated every $\Delta z = 10^{-3}mm$). It was chosen to use, for the calculations, the central wavelength of the Signal range $\lambda = 1200nm$ where the refractive index of PPLN is 2.2. Figure 2.12 reports a symmetric
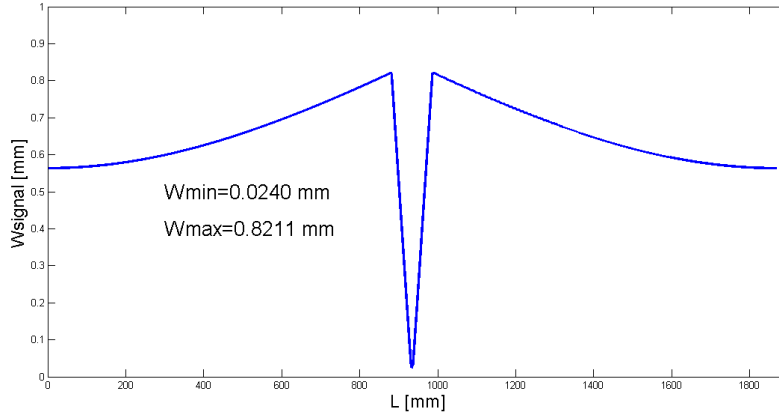

Figure 2.12: Signal spot size inside the resonator at $\lambda = 1200nm$.

behaviour of the spot respect to the center of the resonator, as expected for a symmetric cavity. There is a tight focusing in the middle of the graph due to the effect of the curved mirrors that are focusing the beam inside the crystal.

An important parameter inside the resonator is the **confocal parameter**

of the Signal beam inside the crystal: this value describes how long the depth of focus of the Gaussian beam inside the crystal is. The confocal parameter b is defined as the double of the Rayleigh range $z_R = \frac{\pi n(\lambda) w_0^2}{\lambda}$: the more the confocal parameter value is close to the length of the crystal, the more efficient we are in generating Signal in the crystal. The confocal parameter is equal to:

$$b = \frac{2\pi n\left(\lambda\right) w_0^2}{\lambda} \tag{2.13}$$

Just by zooming Figure 2.12, in order to obtain the spot behaviour inside the crystal, we obtain what the Figure below shows.
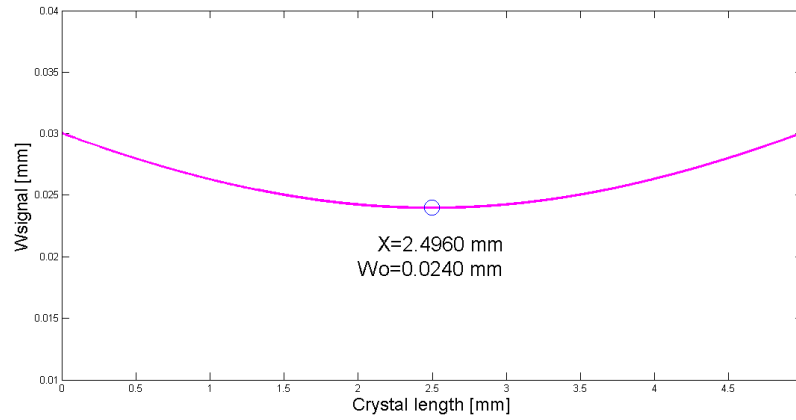

Figure 2.13: Signal spot inside the crystal.

Figure 2.13 reports two information:

1. The focal spot it's in the middle of the crystal, at $x \cong 2.5mm$

2. The dimension of the focal spot inside the crystal is $w_0 = 24\mu m$

Knowing the focal spot of the Signal in the crystal, it's possible to calculate the confocal parameter b and compare it with the crystal length:

$$b = 6.635mm$$

It's close to $5mm$, the crystal length. It shows that, recalling the physical meaning of the confocal parameter, Signal stays focused for all the crystal length. This situation permits to generate Signal efficiently, exploiting the parametric process for whole the crystal length.

Having set the value of the confocal parameter of the Signal, now it's possible to define the Pump parameters.

Input Stage

The role of the Input Stage design is to calculate the optimal Pump beam properties (spot dimension, polarization) to have before entering the resonator. These properties guarantee an efficient generation of the Signal beam through the non-linear crystal. Then in the Set-Up section these properties will be translated in specific optical elements.

The first step consists in ensuring that, while focusing the Pump beam in the crystal, the confocal parameter of the Pump and of the Signal in the crystal must be the same. This situation guarantees the best mode-matching of the beams and also guarantees that the interaction between the beams is all along the crystal length. The confocal parameters' matching between Pump and Signal beam is crucial: the more overlap between Signal and Pump in the crystal, the more Signal is generated in the resonator.

Remembering that the confocal parameter of a Gaussian beam is (Eq. 2.13):

$$b = \frac{2\pi n\left(\lambda\right) w_0^2\left(\lambda\right)}{\lambda}$$

From the previous subsection, the confocal parameter of the Signal is set by the resonator properties to a value of $b = 6.635mm$. Just by imposing this value to the Pump confocal parameter it's possible to find the optimal Pump beam spot $w_0^{opt}\left(\lambda_p\right)$. In order to calculate this, in the following are reported the Pump beam parameters:

- $\lambda_p = 780nm$

- $n_{PPLN}\left(\lambda_p\right) = 2.2$

Replacing this value in the confocal parameter equation, it's easy to find that the optimal Pump beam spot is:

$$w_{0,p}^{opt} = \sqrt{\frac{\lambda_p b}{2\pi n_{PPLN}\left(\lambda_p\right)}} = 19.35\mu m$$

In order to obtain this focal spot for the Pump in the crystal is important to know:

1. The spot dimension of the Pump exiting the laser, $w_{i,p}$

2. The focal of the lens that will focus the Pump on the crystal

Knowing these two parameters we can calculate the magnification to make before the lens in order to obtain in the crystal a $w_{0,p}^{real}$ as close as possible to the optimal one $w_{0,p}^{opt}$.

The Pump spot $w_{i,p}$ exiting the laser was calculted with the Knife-Edge Technique: it consists in slicing a laser beam with a razor and measuring the power of the clipped beam as a function of the razor position. The measured curve is the integral of the marginal distribution, and starts at the total beam power and decreases monotonically to zero power. 30 points were collected and were fit in a Gaussian function using a Matlab code. From the fit the plot in Figure 2.14 was obtained. From the plot it was found that $w_{i,p} = 0.6212mm$.

The setting of the lens' focal was done thinking about avoiding too tight focusing (it can damage the crystal and requires a too short distance between crystal and lens, not possible in the resonator geometry) and also too weak focusing (long focal lengths can't guarantee enough short confocal parameters that can match the Signal's one): a good compromise was to use a lens of $f = 100mm$ ($w_{f=100mm} \cong 39\mu m$, twice the optimal value).

With these two parameters fixed, a rough calculation was performed in order to know what the Pump beam dimension must be before the lens. Knowing from the theory[21] that a collimated Gaussian beam of spot w_{01} generates a spot w_{02} after a lens of focal f:
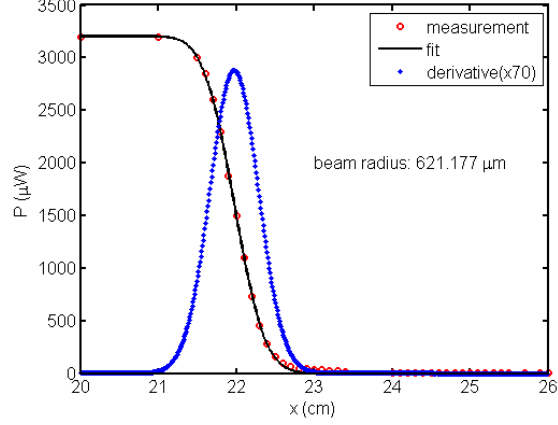
Figure 2.14: Knife-Edge measurement fitting with Matlab.

$$w_{02} \cong \frac{\lambda f}{\pi w_{01}} \qquad (2.14)$$

the $\cong$ symbol is due to the fact that this formula is true when the Rayleigh Range associated to w_{01} is much greater than the focal length f of the lens[21]. In our case:

$$z_{R,1} = \frac{\pi w_{01}^2}{\lambda}$$

without any magnification before the lens $z_{R,1} \cong 1554 mm >> f$. We can calculate which should be the beam spot (w_{01}) before the lens in order to obtain in the crystal $w_{0,p}^{opt}$ as it follows, from Eq. 2.14:

$$w_{01} = \frac{\lambda f}{\pi w_{0,p}^{opt}} \cong 1.283 mm$$

Knowing w_{01} and $w_{i,p}$ we can calculate the right magnification to make before the lens:

$$M = \frac{w_{01}}{w_{i,p}} \cong 2.07$$

This means that a 2x telescope suits almost perfectly the requirements.

After these rough calculations explained just above a Matlab code, using ABCD matrices, was done in order to calculate more accurately the Pump

56

beam spot in the crystal. The calculations were performed with the same method adopted in the previous subsection for the Signal spot in the resonator. This value ($w_{0,p}^{real}$) should be then compared with $w_{0,p}^{opt}$.

In Figure 2.15 it is represented the Pump beam path with all the optical elements:
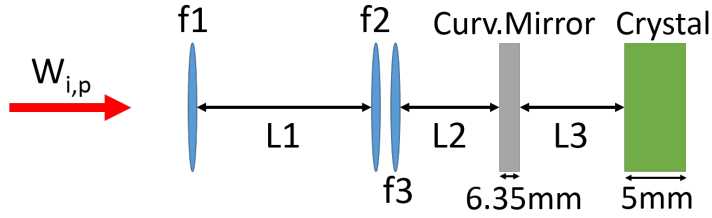

Figure 2.15: Pump beam path.

The elements in Figure 2.15 are:

- $f1$ and $f2$, the lenses of the 2x telescope. In the calculation $f1 = 50mm$ and $f2 = 100mm$ were adopted, separated by a distance $L1 = f1+f2 = 150mm$.

- $f3$, the lens focusing the Pump in the crystal. Its value is $f3 = 100mm$.

- The first curved mirror of the resonator (in gray) through which the Pump must pass in order to reach the crystal. This Fused Silica mirror is $6.35mm$ thick and with a refractive index of 1.45 for the Pump wavelength.

- The PPLN crystal in green, which is $5mm$ thick and with a refractive index of 2.2 for the Pump wavelength.

- Distance L3 is fixed by the resonator stability to $\approx 50.37mm$.

- Distance L2 is a parameter that was varied in order to obtain the focal spot of the Pump beam exactly in the center of the crystal. This value it was found to be $44.01mm$, due to the deviation of the beam caused by the presence of the curved mirror.

The following Figure reports the result of the calculations, where the x axis represents the crystal length.
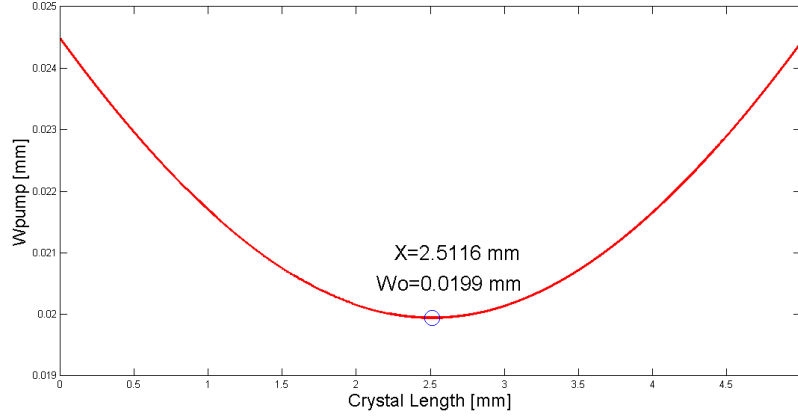

Figure 2.16: Pump spot size inside the crystal.

Figure 2.16 shows that the spot is perfectly centered in the crystal ($X_{focus} \cong 2.5mm$) and the Pump spot dimension is $w_{0,p}^{real} = 19.9\mu m$. The variation between $w_{0,p}^{real}$ and $w_{0,p}^{opt}$ is less than 3%.

With this Input Stage configuration Pump and Signal modes are perfectly matched in the crystal.

2.4   Set-Up

In this section all the optical elements which constitute the OPO will be described. Just in the same way it was done in the Design section, here it's convenient to divide the Set-Up section in two parts: the Input Stage Set-Up and the Resonator Set-Up.

In Figure 2.17 it is reported a sketch of all the elements present in the Optical Parametric Oscillator.
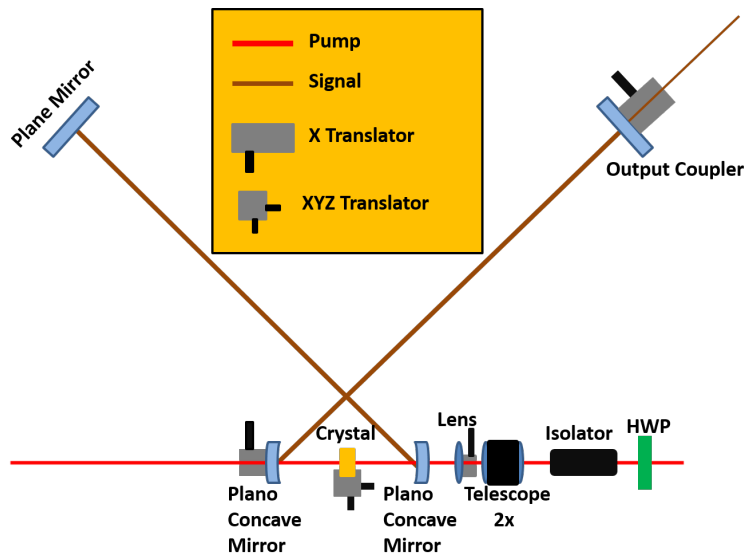
Figure 2.17: OPO's set-up.

2.4.1 Input Stage Set-Up

The Input Stage is composed by:

- An Half-Wave Plate (HWP)

- An Optical Isolator

- A 2x Telescope

- A focusing lens mounted on a translation stage

The HWP and the isolator are used for rotating the polarization of the Pump beam. In fact in order to exploit the biggest non-linear coefficient of the PPLN the Pump must be horizontally polarized (extraordinary axis of the crystal). The role of the isolator is to avoid back-reflection of the Pump from the OPO cavity to the Ti:sapphire cavity (Pump Laser). A back-reflection could cause damages in the Ti:sapphire cavity stopping the mode-locking. An isolator is made by two polarizers with the axis tilted of 45° divided by a Faraday rotator. Figure 2.18 shows that the light coming from the left to

59

the right direction is just rotated in the direction of the polarizer; the light coming from right to left is rotated from 45° to horizontal and so is stopped by the second polarizer.
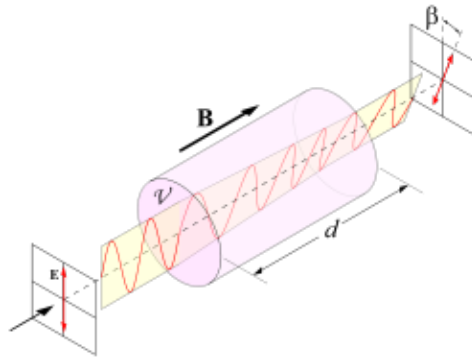

Figure 2.18: Typical layout of an Isolator.

The one that was used is a *IO-5-780-HP-Free-Space Isolator, 780 nm, ⊘ 4.7 mm Max Beam, 40 W Max* from *Thorlabs* (Thorlabs, USA) (2.19).

Figure 2.19: Thorlabs Isolator for $780nm$.

The Pump beam exiting the Ti:sapphire is already horizontally polarized. Figure 2.17 shows that the HWP rotates the Pump polarization to 45° in order to enter with same polarization of the input polarizer of the isolator.

Then the Pump polarization is rotated by the isolator to horizontal again, ready for entering the crystal.

All the information about the 2x telescope are expressed in the previous section; to summarize:

- The first lens $f1$ has a $50mm$ focal

- The second lens $f2$ has a $100mm$ focal

- The two lenses are divided by $L = 150mm$, in this way the magnification $M = \frac{f2}{f1} = 2$

Another important issue is that the focusing lens of $f = 100mm$, whose role is fully described in the previous section, was mounted on a translation stage in order to vary the distance between the crystal center and the lens itself for obtaining the best focus inside the crystal.

2.4.2 Resonator Set-Up

A description of the optical elements inside the resonator, as you can see in Figure 2.17, is reported:

- Two plano concave half-inch mirrors of $R = 100mm$, one of which is mounted on a translator stage

- One plane half-inch end mirror (and two folding mirrors, one on each arm of the resonator, here not represented for simplicity. Their role is fully explained in the Alignment Procedure Appendix.)

- One OC (output coupler) at 2,5% of transmission, located on a translation stage

- The PPLN crystal mounted on a special mount with: a translation stage working in the three directions and a heating system

All the resonator's optical elements were put on a $60mm$ high breadboard (30x60cm) in order to use small pedestals for the optics, this situation guarantees a higher stability in terms of mechanical vibrations.

All the resonator's mirrors were coated by *Layertec* (Layertec, Germany) to be: on the inside resonator face HR (high reflective) in the Signal range $(1000nm - 1400nm)$ and low reflective in the Pump range $(600nm - 900nm)$, on the rear side AR (anti reflection) coated at the Pump wavelength $(600nm - 900nm)$. This situation guarantees a SRO (Singly Resonant Oscillator) in the Signal range, without Pump and Idler powers inside the cavity. The OC was on the rear side AR coated at the Signal wavelength, to avoid losses in the extraction.

The two curved mirrors have a special "C" mount in order to make easier to steer the beam to the folding mirrors with a small angle $(6° - 7°)$. This configuration avoid the astigmatism of the Signal beam caused by big folding angles. In Figure below there is a sketch of the mount structure.
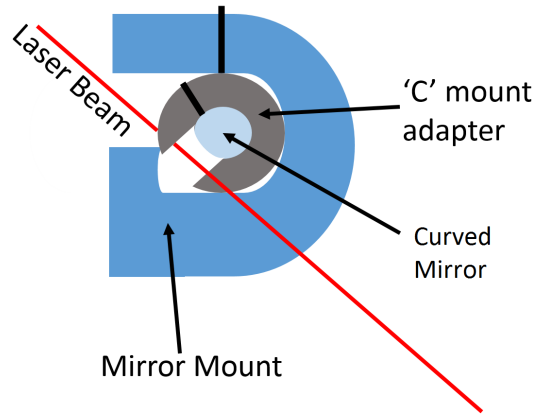

Figure 2.20: Curved mirrors' mount structure.

The PPLN crystal has a special mount, as the one in Figure 2.21. This mount permits to heat the crystal with a heater and to control the temperature with a sensor through a hole near the crystal, as in Figure 2.21. The temperature tuning and control was done using an *ITC 503* temperature controller by *Oxford Instruments* (Oxford Instruments, USA).
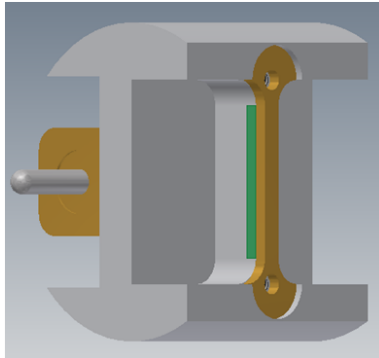
Figure 2.21: PPLN crystal mount with the resistor on the left in gold color and the crystal in the center in green color.

As a sensor was used a K-type thermocouple of Chromel/Alumen made by *RS Components* (RS Components, USA): $1.5mm x 1.0m Type K MiT/c$, probe temperature range $-40^\circ C$ to $+1100^\circ C$ (our working range is from $80^\circ C$ to $200^\circ C$).

Figure 2.22: K type thermocouple.

As a heater was used a resistor *HS10 100R J* made by *Arcol* (Arcol, UK), delivering $5.5W$ to the maximum with a nominal resistance at $25^\circ C$ of 100Ω.

Figure 2.23: Resistor picture.

After having calibrated the sensor, the P.I.D. (Proportional Integral Derivative) values of the temperature controller were set experimentally in order to have fast response of reasonable time in respect of the application.

Concluding, the translation stages were mount on:

- One of the two curved mirror in order to obtain the right distance between it and the crystal.

- The crystal mount for selecting the right grating (translation in the vertical direction) and for placing the facet of the crystal at the right distance from the fixed curved mirror (translation in the beam direction).

Chapter 3

OPO's Characterization

In this chapter the characterization of the OPO source is going to be described. The first section focuses on the possible ways of tuning the output; the second section offers a real characterization of the output in terms of powers and wavelengths.

3.1   Output Wavelength Tuning

There are many ways in order to tune the Signal output of an OPO based on a Periodically Poled Crystal. From the theory it's possible to understand that the output of a parametric process is strongly dependent on the phase-matching conditions, that are strictly correlated to the dispersion curve of the medium used as non-linear crystal.

   The typical way to vary the output is to change the crystal grating period while keeping unchanged the Pump wavelength and the crystal temperature. In this way, by changing the crystal grating Λ_g, we are tuning the Signal by changing the phase-matching conditions: $\Lambda_g = \left[\frac{n(\lambda_3)}{\lambda_3} - \frac{n(\lambda_2)}{\lambda_2} - \frac{n(\lambda_1)}{\lambda_1} \right]^{-1}$. This is the way used to characterize the output of the OPO described in this thesis; in the following section will be shown the experimental results.

   In other occasions it is important to tune the output while keeping constant the grating period: single grating crystals. This kind of tuning permits small and precise variations of the output around the phase-matching

conditions of the grating in use. In this situation there are three possible ways to tune the output:

1. Varying the Pump wavelength (keeping temperature and cavity length constant)

2. Changing the crystal temperature (keeping Pump wavelength and cavity length constant)

3. Varying the cavity length of the resonator (keeping temperature and Pump wavelength constant)

In the first case the variation of the Pump wavelength generates a change in the phase-matching conditions in terms of λ_3: $\Lambda_g = \left[\frac{n(\lambda_3)}{\lambda_3} - \frac{n(\lambda_2)}{\lambda_2} - \frac{n(\lambda_1)}{\lambda_1} \right]^{-1}$.

The second case exploits the dependance of the refractive index of a medium by the temperature: $n = n(T)$. Changing the dispersion curve of a medium means changing the phase-matching conditions. The dependance of the refractive index by the temperature is generally weak; in fact in order to exploit a change in the output there must be a change in the temperature of about $40°C$. In Figure 3.1 it's possible to see the effect of a temperature change of $35°C$ in the phase-matching curves. In this case increasing the
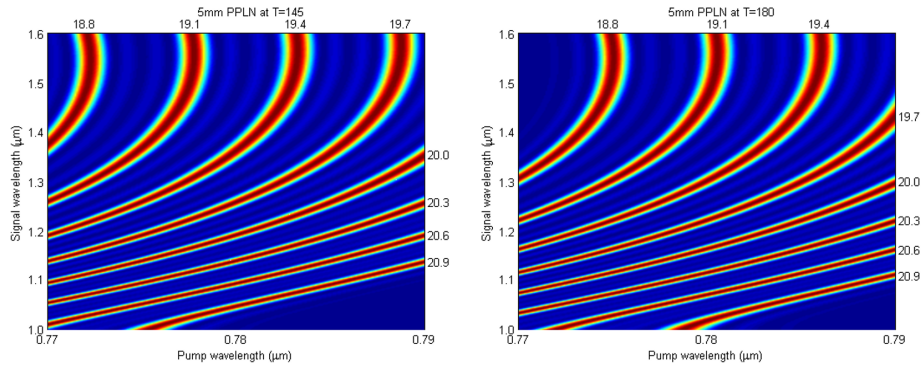

Figure 3.1: 5mm long PPLN phase-matching curves for different gratings at 145 Celsius (left) and at 180 Celsius (right).

temperature of the crystal means lowering the phase-matching curve relative to each grating.

The third case exploits the overlap of the Pump pulse and of the Signal pulse in the crystal. By changing the cavity length we are changing the delay between the Signal and the Pump; in fact the possible variations in the cavity length of an OPO are proportional to the duration of the pulses: the more the pulse is long the more we can vary the cavity length ensuring the overlap between Pump and Signal in the crystal. Generally this tuning method is useful when chirped pulses are present: varying the round-trip time period of the Signal means selecting a different wavelength, inside the Signal envelope, to overlap with the Pump pulse in the crystal. In this way is possible to select which wavelength, inside the phase-matching bandwidth, will experience the biggest amplification in the crystal.

3.2 Output Characterization

In this section the experimental characterization of the output of the OPO source is shown. The characterization measurements were performed on each grating of the PPLN and consist in:

1. Measuring the Signal output for different Pump powers

2. Collecting the spectrum of the Signal output

3.2.1 Output Signal Power and Spectrum

In order to measure, for each grating of the PPLN, the Signal power and spectrum, the subsequent procedure was followed:

1. Fixing the Pump at $780nm$ and the crystal temperature at $110°C$

2. Aligning the cavity with about $100mW$ of Pump power, a value near the threshold of the cavity

3. Optimizing the output in terms of Signal measured power, using an optometer after the OC. The optimization was performed working on the cavity parameters (cavity length, end mirrors angle, distance between the lens and the crystal)

4. Measuring the threshold power of the cavity monitoring the output with an IR viewer

5. Measuring the output power of the optimized cavity for different Pump powers

6. Collecting the spectrum of the Signal with $1880mW$ of Pump power

7. Measuring the depleted Pump power after the crystal in order to know the conversion efficiency of the parametric process

It is important to measure only the near-IR output of the OPO ($1000nm - 1400nm$), filtering all the parasitic mixing present in the cavity and filtering the residual Pump.
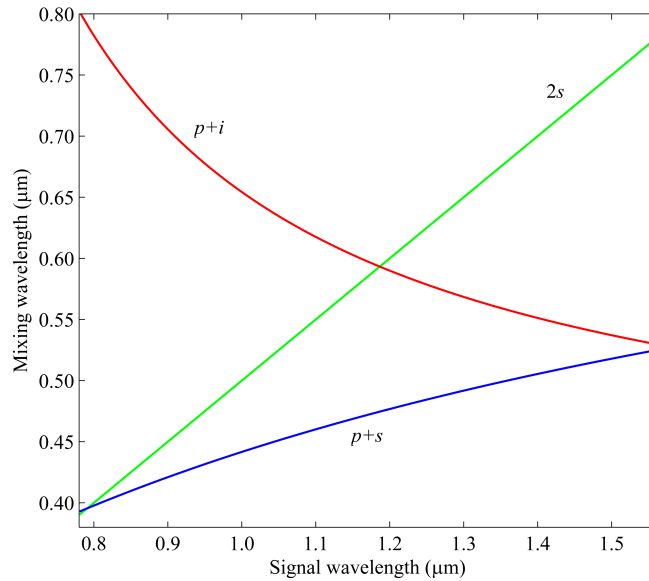

Figure 3.2: Possible wavelength mixing phenomena.

Figure 3.2 reports the possible mixing phenomena (SHG and SFG) present in the cavity. Where $p+i$ is the SFG between Pump and Idler, $2s$ is the SHG of the Signal and $p+s$ is SFG between Pump and Signal. As you can see the biggest part of the mixing processes are in the visible, between $450nm$ and $750nm$. The presence of these parasitic phenomena is due to the high

gain of the PPLN: in this situation also non phase-matched phenomena can oscillate in the cavity. An easy way to attenuate these phenomena is to use cavity mirrors with low reflectance in the visible, that is just what was done in the OPO cavity described in this thesis.

Anyway was used, before measuring the Signal with the optometer and with the spectrometer, a Dichroic Mirror reflecting all the wavelengths above $805nm$: in this way only the near-IR output of the OPO was measured.

The spectrometer used was a *NIRQuest* made by *Ocean Optics* (Ocean Optics, USA); the spectrometer's working range is from $900nm$ to $1700nm$. For the measurements an integration time of $100ms$ was set.

The Pump power tuning was done with the following steps:

1. $P_{in} = 115mW$

2. $P_{in} = 210mW$

3. $P_{in} = 320mW$

4. $P_{in} = 600mW$

5. $P_{in} = 950mW$

6. $P_{in} = 1880mW$

A Pump power limit was set at $1880mW$ in order to avoid crystal damages caused by the intense focused power in the PPLN.

Before starting the analysis of the OPO output for each grating of the PPLN, is important to remember the phase-matching curves for the crystal at $110°C$.
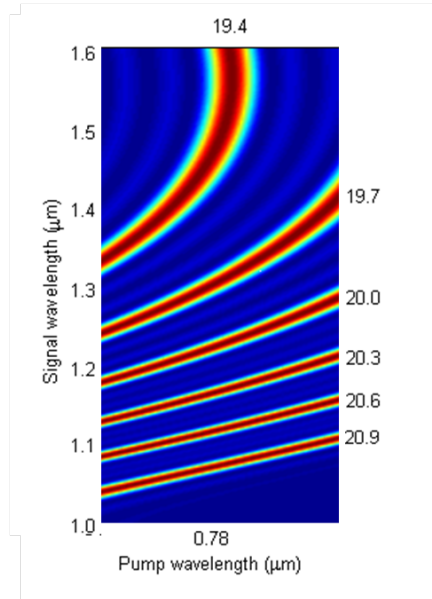
Figure 3.3: Phase-Matching curves for a 5mm PPLN crystal at $110°C$.

From Figure 3.3 it can be found that Signal must be in the following ranges:

- From $1030nm$ to $1100nm$ for the $20.9\mu m$ grating

- From $1100nm$ to $1150nm$ for the $20.6\mu m$ grating

- From $1140nm$ to $1200nm$ for the $20.3\mu m$ grating

- From $1200nm$ to $1300nm$ for the $20.0\mu m$ grating

- From $1250nm$ to $1400nm$ for the $19.7\mu m$ grating

- From $1310nm$ to $1600nm$ for the $19.4\mu m$ grating

For each grating, as well as the output power and spectrum, also the following parameters are shown:

- **Threshold Power**: is defined as the maximum Pump power at which the Signal output power is zero. Above this value there is enough

energy in the resonator to overcome the losses and starts the action of lasing. The threshold power was measured experimentally with an IR-viewer. The IR-viewer was set on the output, while increasing the Pump power. When a flash of light was collected by the viewer the relative Pump power was assigned to be the threshold. The threshold is also calculated using a non-linear trend line to fit the collected power data. In the following is reported only the data fit value.

- **Depleted Pump Power**: is the residual Pump power after the parametric process. From this value is possible to calculate the internal conversion efficiency (η_{int}). This last one is defined as the ratio between $\left(P_p - P_p^{depleted} \right)$ and P_p, where P_p is the Pump power entering the cavity and $P_p^{depleted}$ is the Pump power measured after the parametric process. This value (η_{int}) can be seen as an efficiency of the parametric process. The residual Pump power was measured with $P_p = 1880mW$.

It is important to remember that the cavity gain is not linear; in fact the parametric gain in case of perfect phase matching is $G = e^{2\Gamma L}$ where $\Gamma^2 \approx \omega_s I_p$. The behaviour of the OPO output is expected to be non linear, due to the fact that the gain process of the resonator is non-linear. A non-linear behaviour of the Output power against Input power is expected for those gratings generating lower wavelengths and a more linear behaviour for those gratings generating higher wavelengths. In general the output characteristic of a light source is non-linear near low input powers, due to the fact that there are big losses near the threshold power, and near high input powers, due to the fact that there are high thermal losses that saturates the output.

20.9 um Grating

The behaviour of the output in Figure 3.4 is strongly non-linear: this grating is generating, in fact, the highest Signal frequency ω_s. The output saturates rapidly to $43mW$.

The calculated parameters for this grating are:
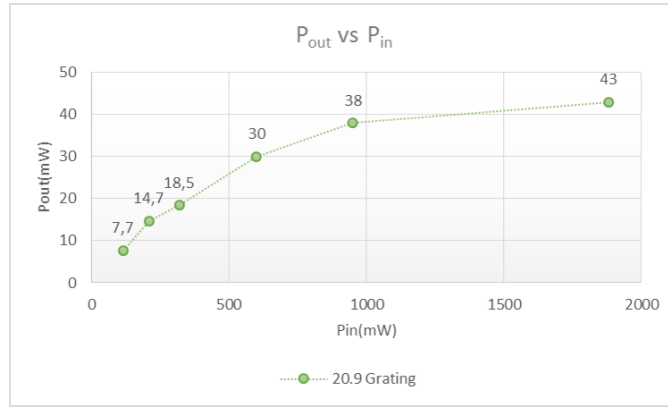
- Threshold with the data fit: $P_{thr}^{data} = 68.5mW$

Figure 3.4: Signal power output as a function of the Pump input power for the $20.9\mu m$ grating.

- Depleted Pump power: $P_p^{depleted} = 150mW$

- Internal Conversion Efficiency: $\eta_{int} = 92\%$
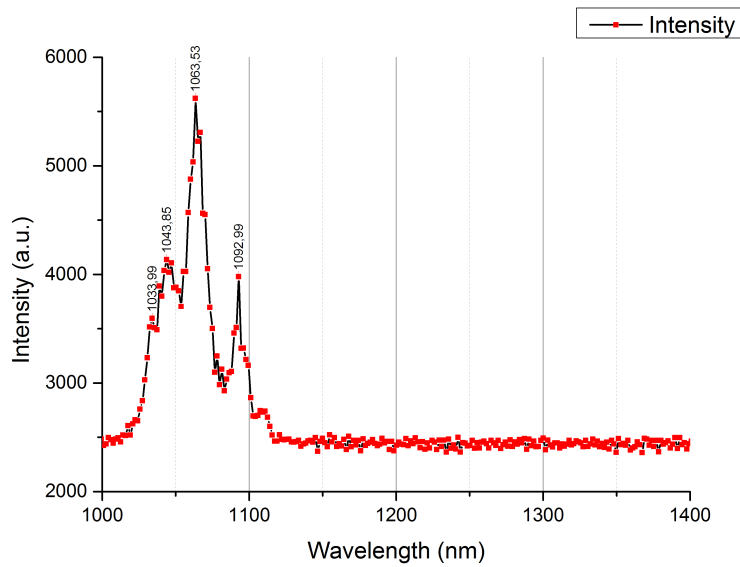
The relative spectrum is reported below in Figure 3.5.

Figure 3.5: Spectrum of the Signal generated by the $20.9\mu m$ grating.

From Figure 3.5 there is:

- A multi-peak structure with the highest peak at $1064nm$.

- A Signal bandwidth of around $50nm$.

It is important to notice that the presence of a multi-peak structure, instead of having a big peak covering all the phase-matching bandwidth, is probably due to the fluctuations in the bandwidth of the reflectivity curve of the cavity mirrors (Figure 3.6).
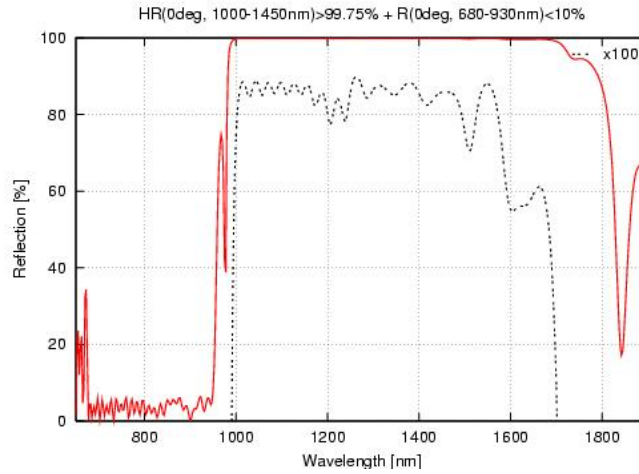

Figure 3.6: Cavity Mirrors' Reflectivity.

Another possibility may be that the coatings have an overall dispersion that has big oscillations: several wavelength regions will have the same dispersion, allowing several narrow-band pulses to propagate with different center wavelengths. This situation will also be seen for all the other spectra of the following gratings: strengthening the hypothesis of defects in the dispersion curve of the cavity mirrors.

20.6 um Grating

The output characteristic is similar to the previous one, due to the high gain of the medium at high Signal frequencies. In this case the highest extracted Signal power is $53mW$.
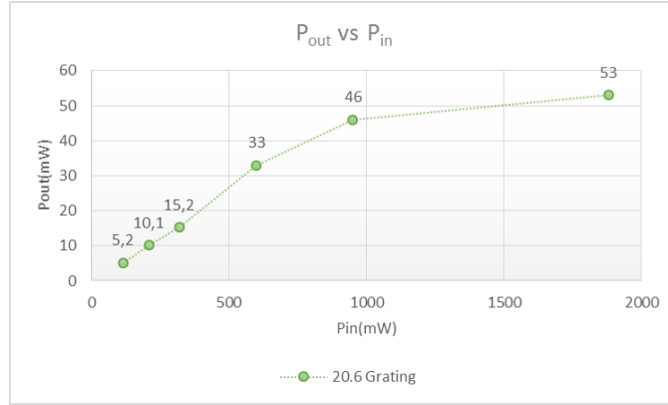
Figure 3.7: Signal power output as a function of the Pump input power for the $20.6\mu m$ grating.

The power parameters of this grating are:

- Threshold with the data fit: $P_{thr}^{data} = 69mW$

- Depleted Pump power: $P_p^{depleted} = 190mW$

- Internal Conversion Efficiency: $\eta_{int} = 90\%$

The spectrum in Figure 3.8 has the following characteristics:

- A multi-peak structure centered at $1125nm$ with four peaks ($1100nm$, $1118nm$, $1134nm$, $1150nm$).

- A $50nm$ bandwidth, as expected from the phase-matching calculations (Figure 3.3).
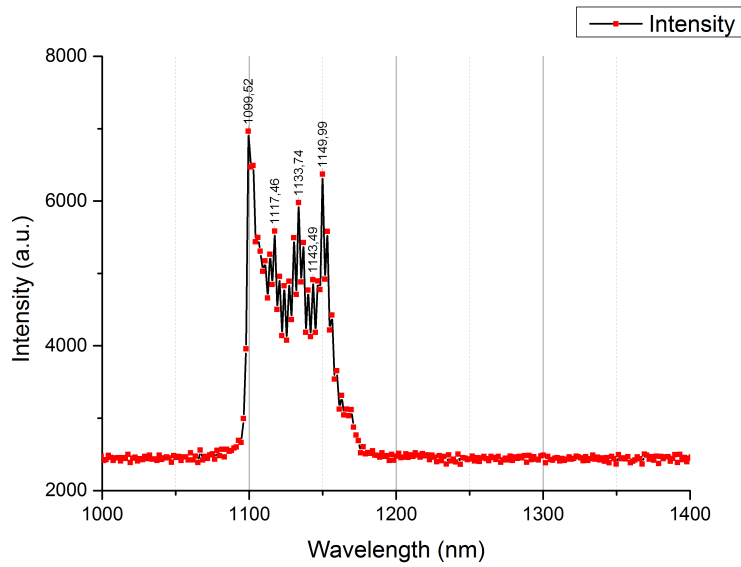
Figure 3.8: Spectrum of the Signal generated by the $20.6\mu m$ grating.
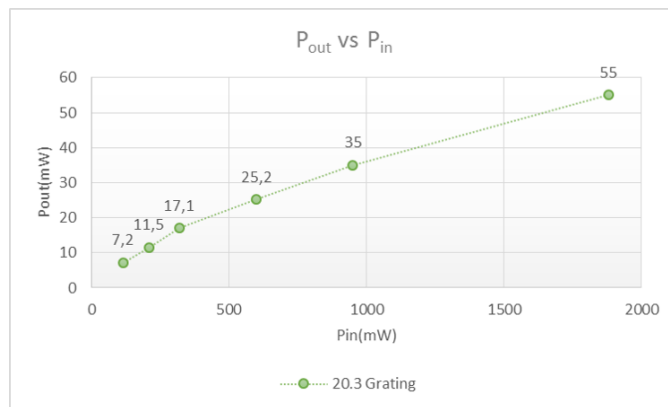
20.3 um Grating

Figure 3.9: Signal power output as a function of the Pump input power for the $20.3\mu m$ grating.

The output in this case is more linear than the two previous cases: the output is not saturating for big Pump powers (according to the fact that the

75

Signal frequency is decreasing). In this case the maximum extracted Signal power is $55mW$.

The power parameters for this grating are the subsequent:

- Threshold with the data fit: $P_{thr}^{data} = 65.7mW$

- Depleted Pump power: $P_p^{depleted} = 170mW$

- Internal Conversion Efficiency: $\eta_{int} = 91\%$

The spectrum in Figure 3.10 reports:

- A multi-peak structure with two high peaks on the sides of the band-width. The peaks are at $1140nm$ and at $1212nm$.

- A Signal bandwidth bigger than $50nm$. Perfectly in agreement with the phase-matching calculations (Figure 3.3).
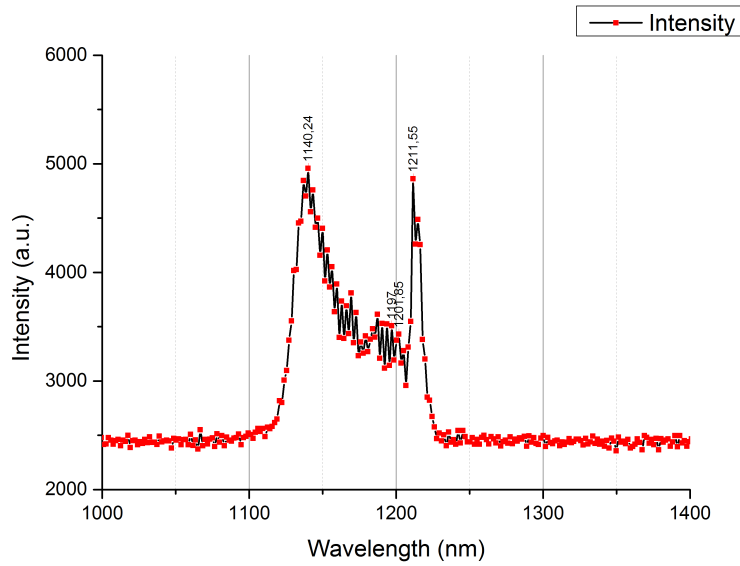

Figure 3.10: Spectrum of the Signal generated by the $20.3\mu m$ grating.

20.0 um Grating

The output generated by this grating has a non-saturated behaviour, as expected with decreasing the Signal frequency. The extracted output power, in this case, arrives to a maximum of $50mW$.
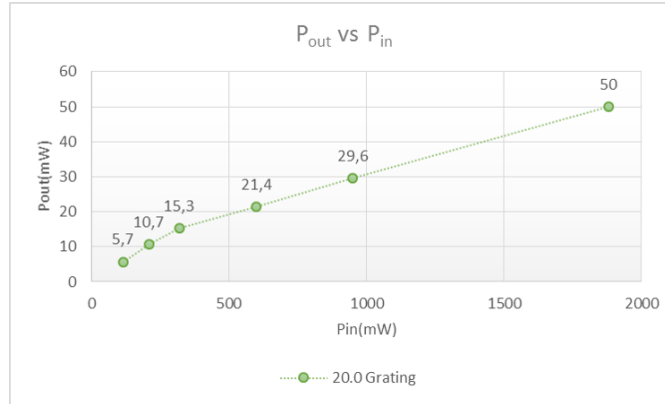

Figure 3.11: Signal power output as a function of the Pump input power for the $20.0\mu m$ grating.

The power parameters are listed below:

- Threshold with the data fit: $P_{thr}^{data} = 65.4mW$

- Depleted Pump power: $P_{p}^{depleted} = 200mW$

- Internal Conversion Efficiency: $\eta_{int} = 89\%$

The spectrum in Figure 3.12 has:

- A two-peaks structure, with peaks at $1236nm$ and at $1252nm$.

- A Signal bandwidth of about $20nm$.

The bandwidth is smaller than the one expected. This fact is probably due to the lowering of the reflectivity curve in this frequency range (Figure 3.6) and/or it can be caused by fluctuations in the dispersion curve of the mirrors. Both of them generates losses in the spectrum of the Signal.
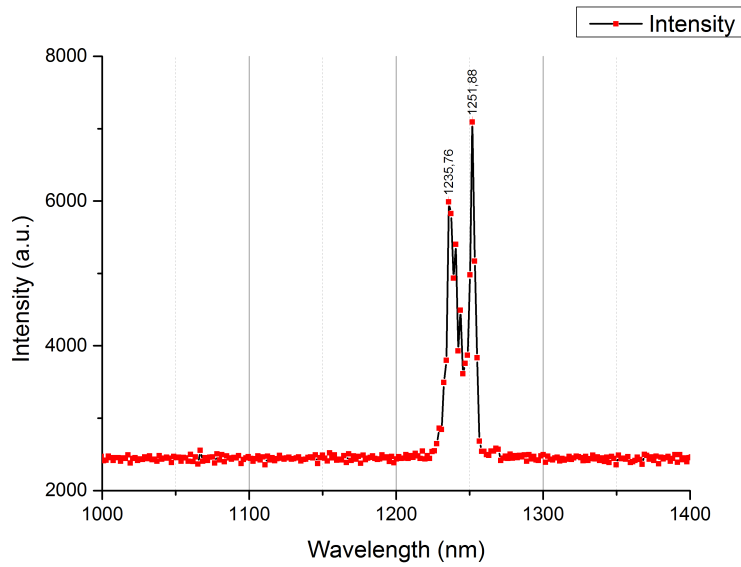
Figure 3.12: Spectrum of the Signal generated by the $20.0\mu m$ grating.
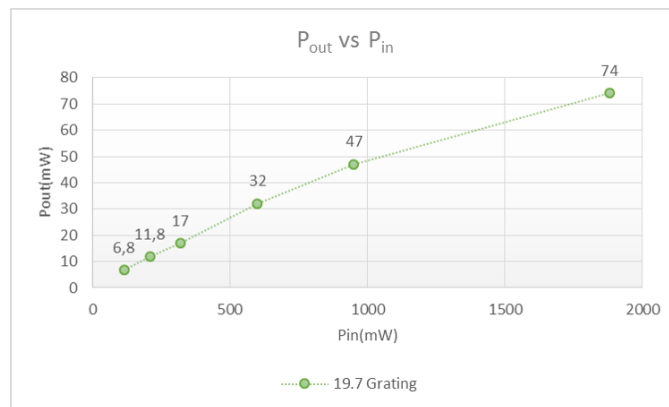
19.7 um Grating

Figure 3.13: Signal power output as a function of the Pump input power for the $19.7\mu m$ grating.

This grating is the most powerful in terms of output; in fact by pumping with $2W$ we can extract about $80mW$: twice the previous cases. This fact is

probably due to the largest phase-matching curve relative to this grating: there is more energy conversion in a bigger bandwidth.
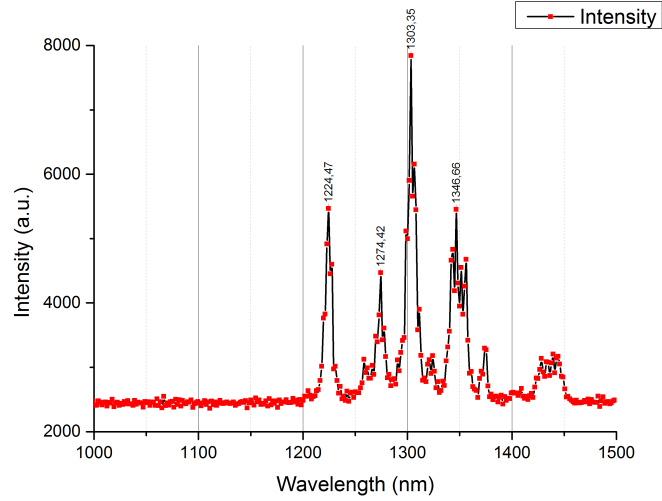
Figure 3.14: Spectrum of the Signal generated by the $19.7\mu m$ grating.

Here are reported the power parameters:

- Threshold with the data fit: $P_{thr}^{data} = 85mW$

- Depleted Pump power: $P_p^{depleted} = 110mW$

- Internal Conversion Efficiency: $\eta_{int} = 94\%$

The spectrum of this grating is reported in Figure 3.14 and manifests:

- A multi-peak structure that extends from $1230nm$ to $1350nm$, centered at $1303nm$. The highest peaks are $1347nm$ and at $1225nm$.

- The Signal bandwidth is around $100nm$, in agreement with the calculations (Figure 3.6).

19.4 um Grating
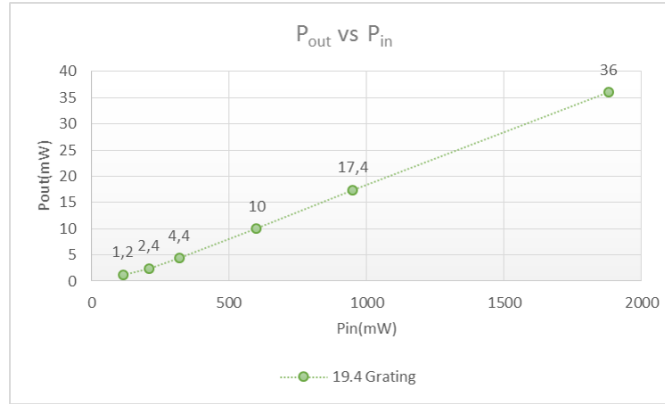
Figure 3.15: Signal power output as a function of the Pump input power for the the $19.4\mu m$ grating.

This grating is the less powerful in terms of output extraction. In fact the highest power obtained is around $30mW$, half the previous cases. This situation is probably due to two facts:

1. If the temperature of the crystal is a little bit lower than $110°C$ the phase-matching curve tends to have the flexion before $780nm$, causing non efficient parametric conversion. Where the phase-matching curve is bent, there are greater fluctuations due to temperature variations.

2. The flexion of the phase-matching curve is the result of being near degeneracy: $\lambda_s = \lambda_i = 2\lambda_p = 1560nm$. In this situation the phase-matching bandwidth is the largest possible and short pulses need a high stability in synchronicity to oscillate. The cavity mirrors have a reflectivity curve for a Signal in the range between $1000nm$ and $1450nm$, causing big losses for this grating. In fact it was difficult to make this grating to oscillate.

The relative spectrum is reported in Figure 3.16.

Below are listed the power parameters:

- Threshold with the data fit: $P_{thr}^{data} = 110mW$
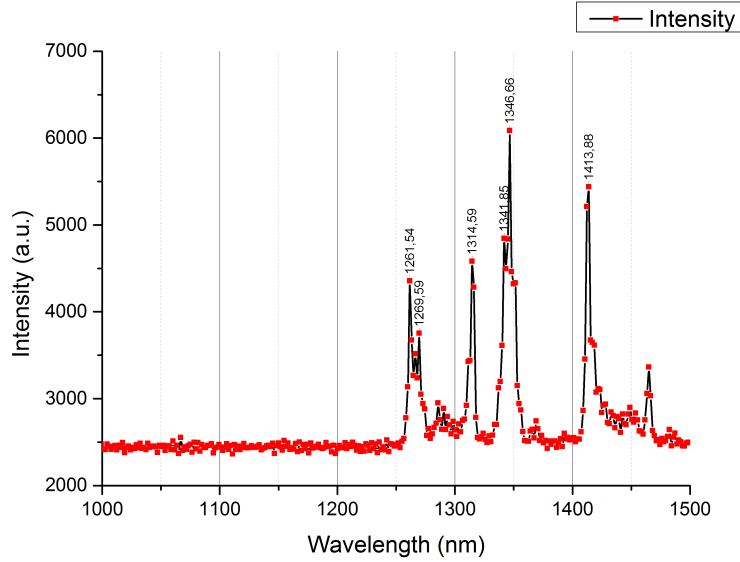
Figure 3.16: Spectrum of the Signal generated by the $19.4\mu m$ grating.

- Depleted Pump power: $P_p^{depleted} = 200mW$

- Internal Conversion Efficiency: $\eta_{int} = 89\%$

From the spectrum (Figure 3.16) there is:

- A large bandwidth with multi-peak structure, centered at $1350nm$. The highest peaks are at $1347nn$ and at $1414nm$.

- A Signal bandwidth that extends from $1260nm$ to $1400nm$. The lower limit of the Signal range is outside the phase-matching calculations; the most probable explanation of this fact is that the crystal temperature was a bit lower than $110°C$, lowering the bottom limit of the phase-matching curve. The upper limit of the Signal range is due to the reflectivity curve of the mirrors that extends from $1000nm$ to $1450nm$.

It's important to notice that larger bandwidth are the most affected by dispersion; in fact the output generated by this grating suffers big losses caused probably by fluctuations of the dispersion curve of the cavity mirrors.

In this way only several narrow bands can be synchronous with the Pump pulse, as Figure 3.16 shows.

Chapter 4

Application to Fluorescence Lifetime Measurements

In this Chapter it is briefly described the use of the OPO source for fluorescence lifetime measurements.

Preliminary measurements on photosynthetic samples were performed using the OPO as the excitation source. In the specific, the measurements were performed on whole cells of different algae species in order to monitor the fluorescence lifetime of Photosystem II (PSII) depending on alga's mutations and alga's stress type. For these samples the excitation is around $650nm$ and the emission has a peak at $685nm$. At room temperature the fluorescence emitted by the cells is almost exclusively derived from PSII.

The properties of PSII, the experimental set-up of and few preliminary results are going to be described in the following sections.

4.1 A Brief Introduction on PSII

The most abundant, and arguably most important light harvesting process on this planet is photosynthesis: the process by which certain organisms convert light into chemical energy. In higher plants, photosynthesis is a two steps process consisting in light-dependent and light-independent reactions. The light-dependent reactions are the first stage of photosynthesis, where light

and water inputs are converted into the energy carrying molecules adenosine triphosphate (ATP) and nicotinamide adenine dinucleotide phosphate (NADPH), which are subsequently used as in the light-independent reactions alongside CO_2 to produce glucose.

In higher plants, algae and in cyanobacteria the light-dependent reactions of photosynthesis take place at thylakoids (Figure 4.1), a membrane-bound compartments within the chloroplast organelles found in leaf cells.

Plant Cell Chloroplast Structure
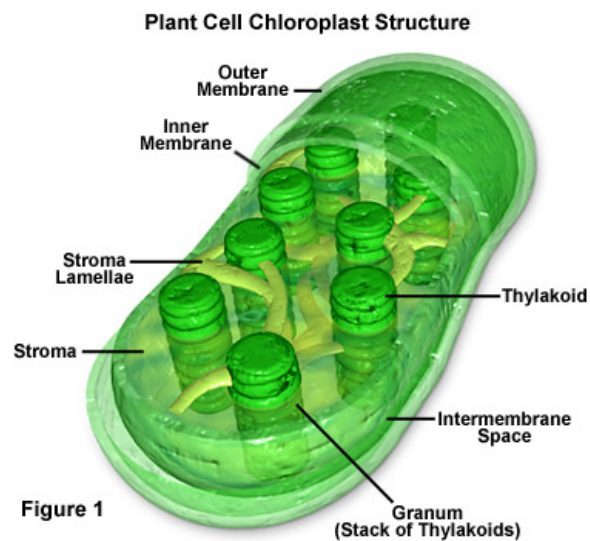
Figure 4.1: Location of thylakoid compartments within the chloroplast organelles.

The thylakoid membrane separates the thylakoid interior, called lumen, from the exterior chloroplast space, called stroma. Multiple protein structures are embedded within the thylakoid membrane (Figure 4.2), and it is within these structures that the light-dependent reactions take place.

Briefly the steps of the reaction are[22]:

- A photon is absorbed by photosystem II (PSII)

- The excited electron is transferred to the plastoquinone structure, thereby oxidising PSII

- PSII is subsequently reduced by the hydrolysis of water present in the
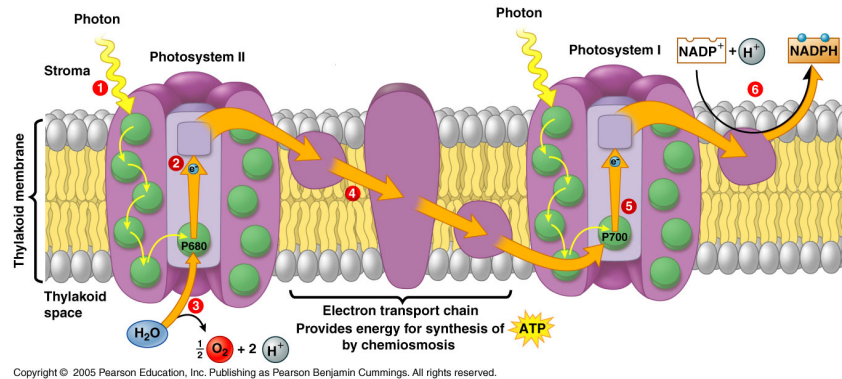
Figure 4.2: Thylakoid membrane protein structure involved in the light-dependent reactions of photosynthesis.

    lumen, liberating molecular oxygen to the environment and protons to the lumen

- The electron is passed along a transfer chain consisting of plastoquinone, cytochrome and plastocyanin structures, before arriving at photosystem I (PSI)

- During transfer from plastoquinone to cytochrome, the energy carried by the electron is used to pump protons from the stroma to the lumen via a further trans-membrane REDOX reaction

- A photon is absorbed by PSI

- The excited electron is transferred to ferrodoxin, oxidising PSI, where it is used to reduce $NADP^+$ to NADPH

- PSI is subsequently reduced by the electron originating from PSII

- The proton gradient developed across the thylakoid membrane during the entire reaction is used by the ATP synthase to convert ADP in the stroma to ATP

It can be seen that the light-dependent reactions are reliant on the sequential absorption of two photons.

Focusing on the PSII structure, there is a reaction center (RC) containing a chlorophyll (Chl) dimer which performs electron transfer to the adjacently located structures: plastoquinone in the case of PSII. Owing to its small cross-section however, the probability of photon absorption by the Chl dimer is very low. The reaction center is therefore bound to pigment containing cofactors to increase absorption, with the absorbed energy being transferred to the reaction center via non radiative processes (eg. FRET), where the energy is used for charge separation. These additional antenna cofactors are denoted core antenna complexes and contain beta-carotene and Chl A pigments. In PSII these antenna cofactors are pigment-protein complexes, called CP43 and CP47. The ensemble of reaction center and inner antennas are known as the photosystem-core (PS-core). Photosystem-core absorbance is further increased by association to surrounding outer LHCs, which again harvest light and transfer energy non-radiatively to the PS-core. The predominant outer LHCs associated to PSII are denoted LHCII. The outer LHCs contain mainly the pigments Chl A and Chl B and xanthophylls.

The bond between the outer LHCs and the chlorophylls causes red shift in absorption for these outer antennas. Their role is to absorb energy in the red spectrum, in order to further increase the absorbance of the PSII [23,24].

4.2   Set-Up and Results

4.2.1   Samples

The experiment was performed on two different types of alga's cells:

- Haematococcus Pluvialis (HP)

- Chlamydomonas Reinhardtii (CR)

For the HP algae there were three kinds of samples:

1. The control sample (abbreviation "HPverde")

2. The sample held without nutrients (mild stress) (abbreviation "HPverde-menoN")

3. The sample subjected to strong illumination (strong stress) (abbreviation "HProsso")

HP is an alga that under stress accumulates a carotenoid (astaxanthin) that has the function of sun screen, thus decreasing the absorption in the UV-blue part of the solar spectrum[25]. That is why it is necessary to analyze these samples in the red part of the spectrum. The idea was to monitor, in function of the stress applied to the samples during the growth, the variations in the fluorescence lifetime of the photosynthetic subunits of PSII.

For the CR algae there were two kinds of samples:

1. The wild type sample (control sample) (abbreviation "CRWT")

2. The mutant sample (abbreviation "CRN2")

CR is the typical green alga. Here the aim of the measurement was to monitor, in function of the mutation, the variations in the fluorescence lifetime of the photosynthetic subunits of PSII.

It was performed a Time Resolved Photo-Luminescence (TRPL) measurement because the fluorescence lifetimes of the photosynthetic subunits are indicative of the efficiency of the energy transfer in the PSII. The samples were flushed into a cuvette through the use of a peristaltic pump: this set-up guarantees, thanks to the continuous flow of samples, the possibility of *in vivo* measurements.

4.2.2   Set-Up

Excitation

The OPO was used to generate a $1300nm$ output by pumping with $780nm$. By making frequency doubling with a Type I BBO crystal cut for $1200nm$, the excitation pulses at $650nm$ and at a repetition rate of $80MHz$ were obtained. The spectrum of the OPO (previous chapter) is centered at $1300nm$ when the $19.7\mu m$ grating is used. The alignment of the OPO on the $19.7\mu m$ grating was performed, with the help of an IR spectrometer, working on the optimization of the Signal spectrum around $1300nm$. The optimization consists in using

the cavity length tuning in order to maximize the spectral components of the Signal around $1300nm$; this situation guarantees an efficient SHG. The Signal exiting the OPO was $\approx 40mW$ and then, after the BBO crystal and a narrow filter around $650nm$, it was few μW.

Acquisition

The acquisition system is based on a steak camera (Hamamatsu C5680, Japan) and an imaging spectrograph (Princeton Instruments Acton SP2300i, USA).

A streak camera is a detection device capable of having both high temporal resolution (about $2ps$) and high spectral resolution (depending also on the type of grating used before entering the device). The basic operation scheme of a streak camera is reported in Figure 4.3.
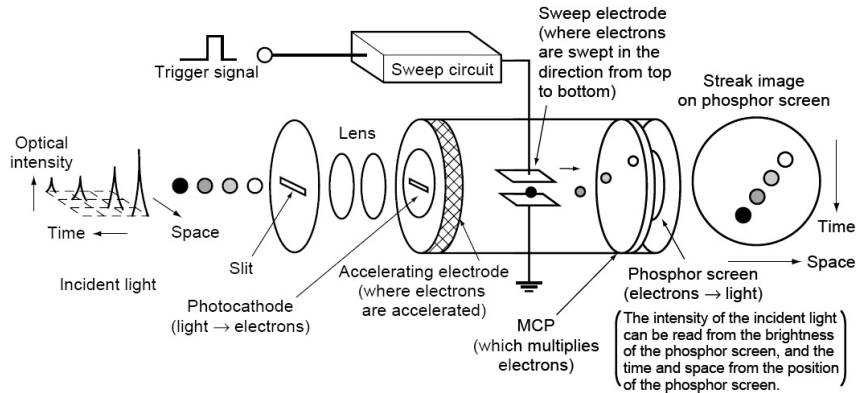

Figure 4.3: Streak Camera schematic of the operation.

Schematically we have these steps:

1. The incident photons are transformed in electrons by the photocathode

2. The generated electrons are accelerated by the accelerating electrode

3. The sweep electrodes deviate the electrons, in the order of arrival, from top to bottom

4. The deviated electrons are multiplied by the Multi-Channel Plate (MCP)

5. The electrons arrive to the phosphor screen which transforms electrons in photons

6. The light generated by the phosphor screen is captured by a CCD

The intensity of the incident light can be read from the brightness of the phosphor screen, while time and space from the position of the emitted light from the phosphor on the screen.

The *Hamamatsu C5680* Steak Camera has two types of sweep control unit:

- Synchroscan

- Slow sweep

Sweep triggering is provided by splitting part of the Pump beam on a stabilized silicon fast photodiode coupled to variable electronic delays. The principal difference between the two sweep units is the form of time-varying voltage applied to the deflection electrodes.

The voltage sweep provided by the Synchroscan unit is sinusoidal with quasi linear electron deflection being measured around the maximum voltage gradient. The benefit of such a scheme is that accurate control of the sinusoidal frequency effectively eliminates sweep-to-sweep trigger jitter, thereby obtaining a temporal resolution, on integrated measurements, of $2ps$ at best. This high resolution (the resolution it's always 1% of the temporal window) comes at the reduction of the usable temporal window to $2ns$, due to the sweep non-linearity.

The Slow Sweep unit provides an approximately linear voltage ramp, leading to linear electron deflection. The temporal resolution in this modality is mainly limited by the electronic jitter in the trigger signal from one sweep to the next. A $50ps$ plus 1% of the the temporal window adopted for the measurement resolution is attainable on any integrated measurement. This modality is used in conjunction with the Pulse-Picker (in order to decrease

the Repetition Rate of the Pump source) for measurements of time ranges longer than $2ns$.

Before entering the streak camera there is the imaging spectrograph. This set-up (the sequence of spectrograph and streak camera) permits to convert the spatial resolution of the streak camera into the spectral resolution. The spectrograph deflects the different spectral components of the entering light at different angles. The spectrograph is equipped with two visible and one near-IR reflecting gratings to provide broadband spectral resolution.

An example of the experimental data collected using the acquisition set-up is reported in Figure 4.4.

Figure 4.4: Example of data collected using the acquistion set-up.
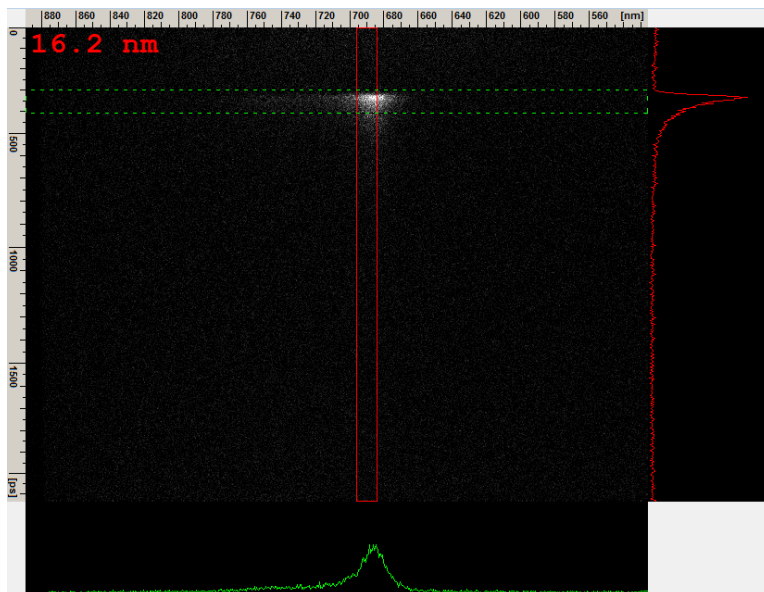
The vertical axis of the image is the time, while the horizontal one is the spectrum. It's possible to select:

1. A time window, in order to monitor the spectrum integrated in the time interval adopted (colored in green in Figure 4.4).

2. A spectral window, in order to monitor the kinetics integrated in the spectral range adopted (colored in red in Figure 4.4).

For the measurements the Synchroscan unit was used because the fluorescence lifetimes to monitor had decay time constants around hundreds of picoseconds[23]. The range adopted on the streak camera was a time window of $2ns$, with a time resolution of $20ps$ (1 % of the time window) at the best. A $\frac{50 grooves}{mm}$ visible reflecting grating was equipped on the spectrograph during the measurements.

4.2.3   Results

Instrument Response Function (IRF)

Before starting to analyze the data collected during the measurements is important to discriminate whether the pulses of the excitation line were of comparable duration with the resolution of the streak camera.

A method capable of giving information about the duration of the pulses entering an acquisition system in comparison to the time of response of the acquisition system itself is the Instrument Response Function (IRF). The IRF is defined as the function describing the system response when it is excited with a delta pulse (a pulse with temporal duration much shorter than the time response of the system). Mathematically it is possible to express the IRF by the use of the convolution product: $f(t) = IRF(t) \otimes Pulse(t)$. Where $f(t)$ is equal to the IRF when $Pulse(t)$ is a delta pulse. Generally it's useful to define the IRF as the FWHM (Full Width at Half Maximum) of the time response of the system.

The IRF of the streak camera was measured experimentally sending directly the Pump pulses, whose duration ($150fs$) is much lower than the time of response of the instrument, into the streak camera. This method allows one to estimate an IRF of about $20ps$ using a $2ns$ temporal window for the acquisition.

Using the same temporal window of acquisition, it was performed the IRF of the streak camera using the scatter, through a cuvette filled with water, of the excitation pulses coming from the OPO at $650nm$. In Figure 4.5 it is reported the system response.

Via software it is possible to fit with a Gaussian function the time depen-
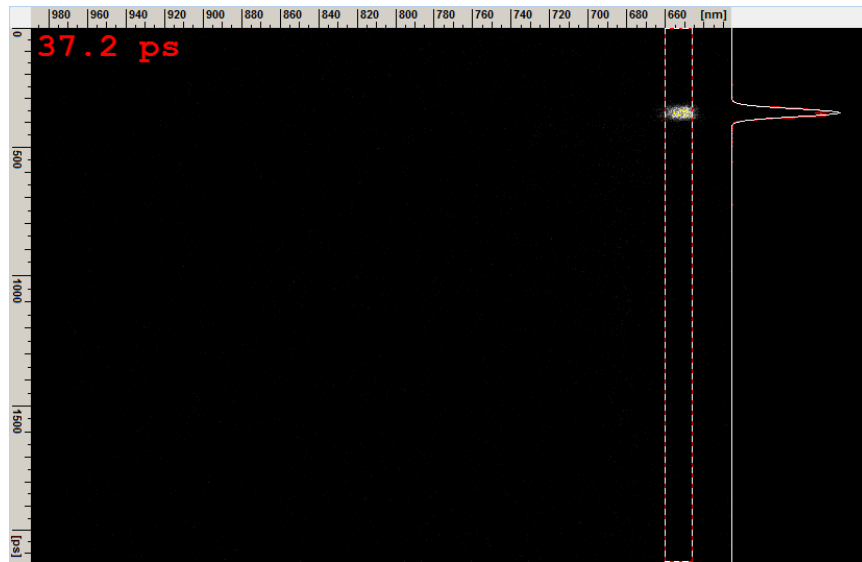
Figure 4.5: IRF of the streak camera when exposed to the $650nm$ pulses.

dent function (system response), collected by the streak camera, integrated in a specific spectral range. From the fit (the white Gaussian function in Figure 4.5) it was estimated a FWHM of the system response of about $37ps$. This value is greater than the one given by sending directly the Pump pulses into the streak camera, because the effect of the scatter through the water is to enlarge the pulse duration. In fact by making the IRF using the scatter of the Pump pulses, same results for the estimation of the system response were obtained. Thus ensuring that the duration of the OPO pulses is much shorter than the time response of the system.

In this case, using a $2ns$ temporal window and working with the presence of scatter induced by the samples immersed in water, a resolution of the system of about 1.9% of the temporal window (generally the best obtainable resolution is 1% of the temporal window) is obtainable. This resolution seems reasonable in comparison both to the temporal window adopted and both to the fluorescence lifetimes to monitor.

Experimental Results

The fluorescence emission spectra of the algae (CR and HP types) are reported in Figure 4.6. The spectra are collected from $680nm$ to $750nm$ and are integrated in a time interval starting from the excitation until the end of the temporal window of acquisition of $2ns$. All the spectra have the emission
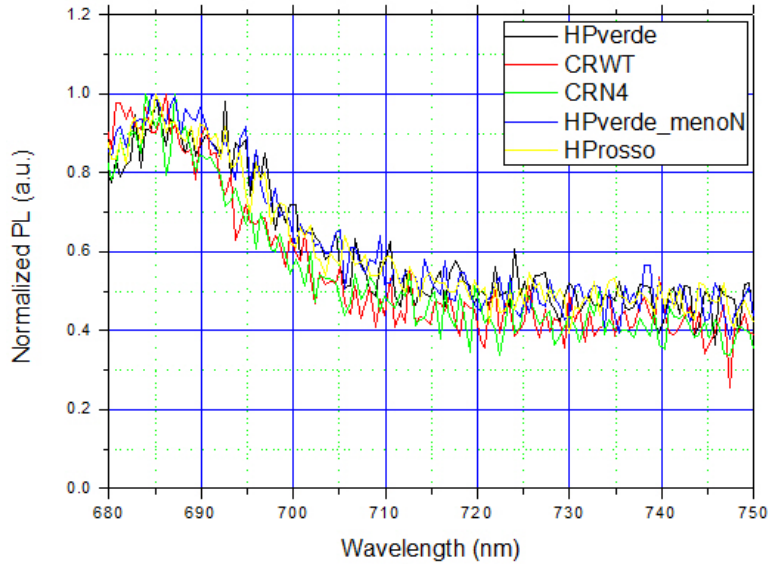

Figure 4.6: Time resolved emission spectra collected by the streak camera.

peak at $685nm$ with a broad band of fluorescence. The collected spectra are not centered at $685nm$ in order to let the excitation wavelength ($650nm$) outside the acquisition range.

In Figure 4.7 it is reported the dependance of the fluorescence emission of the photosynthetic subunits of PSII on the intensity of the stress applied, during the growth, to the alga's cells. The time resolved fluorescence is normalized to the peak and it is integrated in the spectrum from $680nm$ to $750nm$.

From Figure 4.7 it seems that the kind of stress applied to the cells influences the fluorescence lifetimes. In fact Figure 4.7 shows that those forms that are grown under mild stress have shorter fluorescence lifetimes in comparison to the wild type. This means that the efficiency of energy
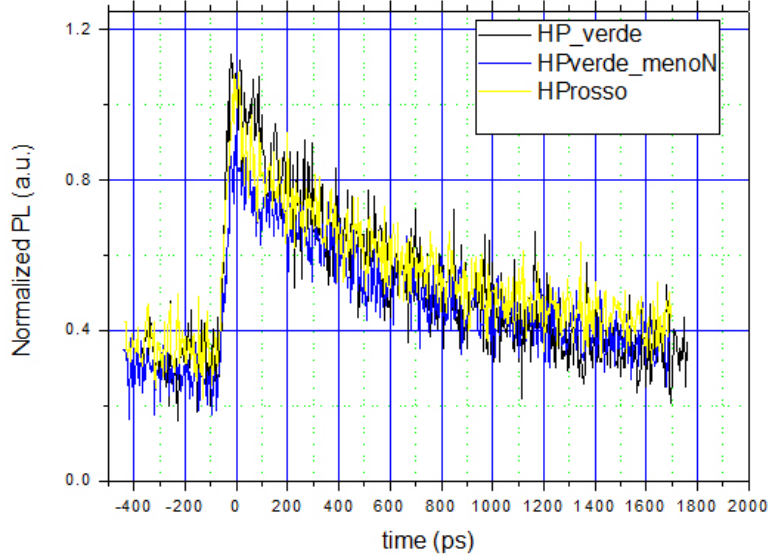
Figure 4.7: HP kinetics.

transfer of the photosynthetic subunits in algae is dependent on the intensity of the stress applied to the cells. The fluorescence emission seems to be not influenced by the strong stress applied to cells.

A data fit was performed on these fluorescence measurements, using, as the theoretical fit function, a biexponential:

$$PL\left(t\right) = PL_0 + A_1 e^{-\frac{t}{\tau_1}} + A_2 e^{-\frac{t}{\tau_2}}$$

where PL_0 is the backround value of PL, A_1 and A_2 are the amplitudes of the two exponentials, τ_1 and τ_2 are the decay constants of the two exponentials. From the estimation of these parameters it is possible to understand and to quantify the dependance of the mutation on the efficiency of fluorescence emission. Here the fitting parameters for these data are reported:

- "HPverde": $A_1 = 0.2$ and $\tau_1 = 123ps$; $A_2 = 0.6$ and $\tau_2 = 865ps$

- "HPverdemenoN": $A_1 = 0.1$ and $\tau_1 = 10ps$; $A_2 = 0.5$ and $\tau_2 = 734ps$

- "HProsso": $A_1 = 0.2$ and $\tau_1 = 26ps$; $A_2 = 0.5$ and $\tau_2 = 795ps$

The stress applied to the cells influences mostly the fast component of the fluorescence decay. In fact the control sample has a 10 times greater decay constant (τ_1) than the mild stress type and 5 times greater than the strong stress type. The slow component of the fluorescence decay seems less influenced by the intensity of the stress applied to the samples; in fact the variation in the decay constant is around 15% between the control sample and the mild stress type. Thus leading that the stress applied to the samples manifests itself in the short time period of the fluorescence emission.

Knowing that the stress applied to the cells influences the fluorescence, it is possible to find which kind of genetic mutation could inhibit the occurrence of stress as inefficiency in the fluorescence emission. From this motivation, genetically modified cells of algae were studied. The samples reported below have a specific genetic mutation and the idea was to monitor if this kind of mutation is responsible of the lowering in the efficiency of PSII.

The dependance of the fluorescence emission of the photosynthetic sub-units on the mutation of the alga's cell is shown in Figure 4.8.
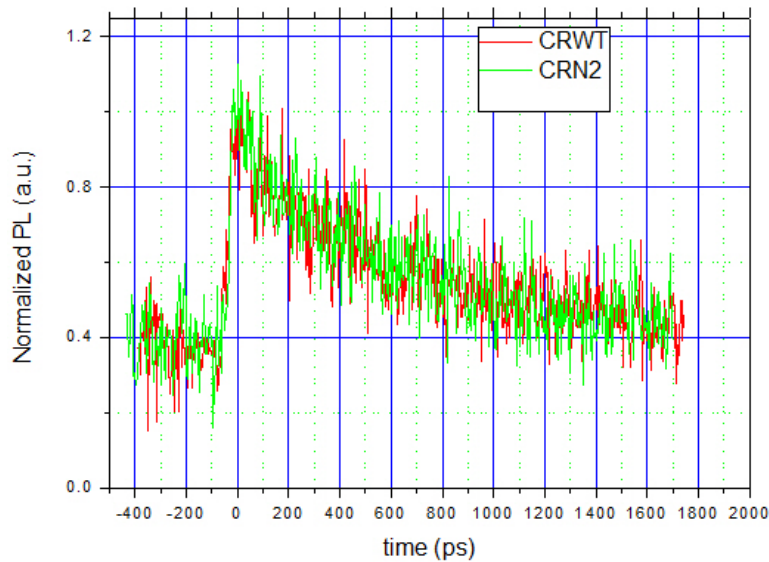

Figure 4.8: CR kinetics.

The fluorescence emission seems to be independent from the mutation of

95

the alga. Thus ensuring that the mutation is not influencing the efficiency of energy transfer in PSII. In fact the two fluorescence decays are overlapped in the acquisition window.

On these data the same method of fitting of the previous ones was applied. Below the fitting parameters are reported:

- "CRWT": $A_1 = 0.1$ and $\tau_1 = 59ps$; $A_2 = 0.5$ and $\tau_2 = 759ps$

- "CRN2": $A_1 = 0.2$ and $\tau_1 = 39ps$; $A_2 = 0.5$ and $\tau_2 = 664ps$

The variation in the fluorescence lifetime, for the predominant slow component, in dependence of the mutation is less than 3%. Thus ensuring that this genetic mutation is not influencing the fluorescence emission of the photosynthetic subunits in PSII.

For conclusion, these preliminary results show a dependance of PSII efficiency on the stress level.

Chapter 5

Conclusions and Future Perspectives

In this thesis an Ultrafast Optical Parametric Oscillator tunable from 1000nm to 1400nm for Time Resolved Photoluminescence (TRPL) measurements has been designed and implemented. In particular the design of the cavity has been made, then the source has been built and it was finally characterized. As the conclusion of this project, an application of the source in measurements on Light Harvesting Complexes of photosystem was performed. At the end of this work the OPO appears to be functional and usable for TRPL measurements. The biggest criticality that was found, for this source, it is represented by the obtainable output power.

The possible improvements here reported are the result of different issues: power issues, tuning issues, stability issues and versatility issues. We can divide the issues in two categories:

1. **Performance Issues**: regarding the demands of stability, power and tunability in order to make the source reliable for measurements on samples.

2. **Functional Issues**: concerning the simplification and the compaction of the source.

The possible performance improvements to adopt are the following:

- Enclosing the OPO in order to make it more stable.

- Using a 15 % Output Coupler [18] (OC) in order to extract more Signal power from the cavity for an external SHG.

- Using an internal SHG crystal in the cavity for doubling the Signal.

- Using a Fan-Out non linear crystal, instead of the multi-grating solution. Thus allowing continuous tunability.

The OPO source is very sensitive to air fluctuations inside the resonator caused by movements around it. By enclosing the OPO, putting a plexiglass box around it, a better stability in terms of output power and spectrum can be achieved. In fact if the cavity length L_{cav} is:

$$L_{cav} = L_1 n_{air} + L_{crystal} n_{crystal} = 1873.7 mm$$

When n_{air} is changing (eg. air fluctuations) also the cavity length is changing. The synchronicity between Pump repetition rate and Signal repetition rate is crucial for the OPO operating regime: variations in the cavity length from the optimal situation cause the cessation of the lasing oscillation.

Changing the 2.5 % OC with a 15 % OC have two effects:

1. Increasing the threshold power of the cavity because we are increasing the cavity losses.

2. Increasing the output power.

Theoretically the increase factor, from the previous case with the 2.5 % OC, is proportional to (linear approximation):

$$M \approx \frac{15}{2.5} = 6$$

In this way the threshold of the cavity will be about six times greater than the previous situation, but the output power will increase of the same factor ensuring more useful power for doubling the Signal exiting the OPO. Assuming that we have, at most, $50 mW$ of Signal power with the 2.5 %

OC and assuming that with an external SHG crystal we can obtain $5\mu W$ of second-harmonic (efficiency $\eta = 10^{-4}$); with the 15 % OC solution we can obtain around $300mW$ of Signal power and $300\mu W$ of its second-harmonic. This solution will increase of a factor 60 the possible SHG obtainable. These rough calculations exploit that the SHG efficiency increase linearly with the incident power.

The internal cavity SHG solution would be the best solution in terms of obtainable power in the visible. In fact having a 2.5 % OC and $50mW$ of output power means that inside the cavity we have around $2W$ of Signal power. In the approximation of no cavity losses it's possible to say that doubling the Signal inside the cavity guarantees, using a SHG crystal with $\eta = 10^{-2}$ ($\eta_{2W} = \frac{2W}{50mW}\eta_{50mW} \approx 100\eta_{50mW}$), $20mW$ of its second-harmonic. This ensuring a 4000 times greater SHG than the actual situation. The cavity configuration would be the following reported in Figure 5.1.
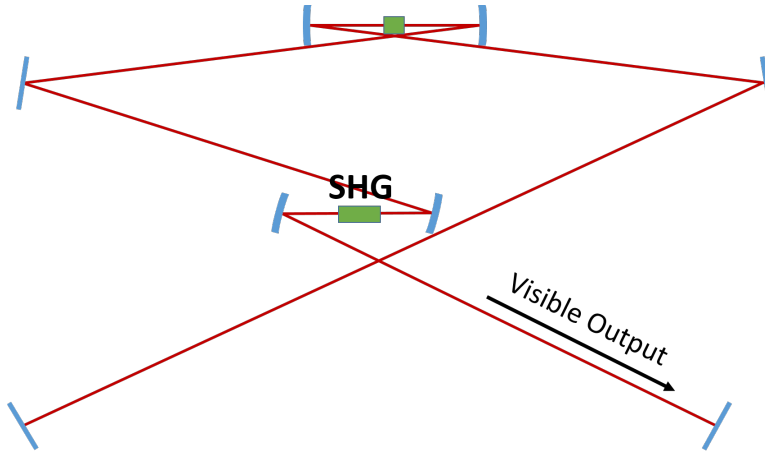

Figure 5.1: Cavity configuration for a linear cavity OPO with internal SHG.

The cavity in Figure 5.1 has the same structure of the OPO described in this thesis, with the only difference that there are two extra curved mirrors in order to focus the Signal into the SHG crystal. It's important to make an HR coating for the visible on the second new curved mirror in order to collect all the second-harmonic without losses after the crystal. There is only one issue in this new cavity configuration: the visible is generated in both directions

inside the cavity, while it is possible to collect it only in one direction. This problem can be solved using a Ring-Cavity configuration.

Using a multi-grating crystal it is possible to have tuning, but not continuously. This is due to the fact that the variation between two adjacent gratings is discrete in terms of poling period. An easy way to avoid this problem is to use a Fan-Out crystal, shown in Figure 5.2.
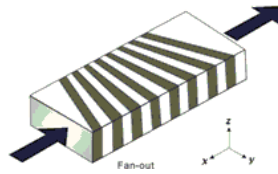

Figure 5.2: Fan-Out Crystal geometry.

With this crystal geometry, by moving the beam in the lateral direction, a continuous variation in the grating period can be exploited. In fact the phase-matching curves, using a $1mm$ long crystal and using the same conditions of Pump and Signal range relatively to this thesis, result to be those in Figure 5.3. In this case it is possible to cover all the Signal range continuously.
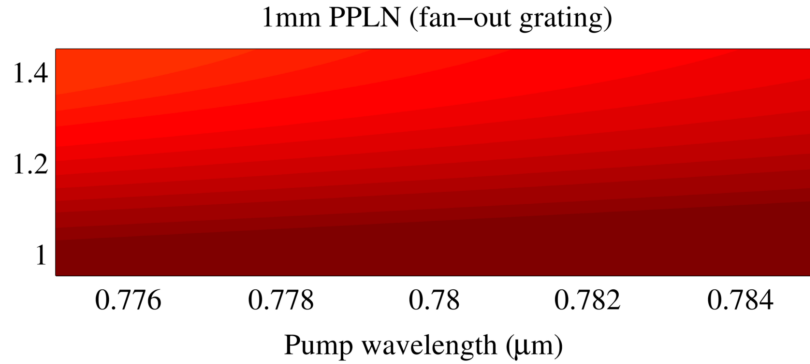

Figure 5.3: Phase-Matching curves for a 1mm long PPLN with fan-out grating.

The functional improvement to adopt is based on the idea of having a more compact source, which could contain both the resonator and the input stage on the same breadboard. This condition guarantees an easier way to control independently both the Chameleon Pump source and the OPO source. The cavity is in the shape of X arranged on a rectangular breadboard, so it's possible to use the two triangular spaces where the beam is not passing. What should be the final result is reported in Figure 5.4.
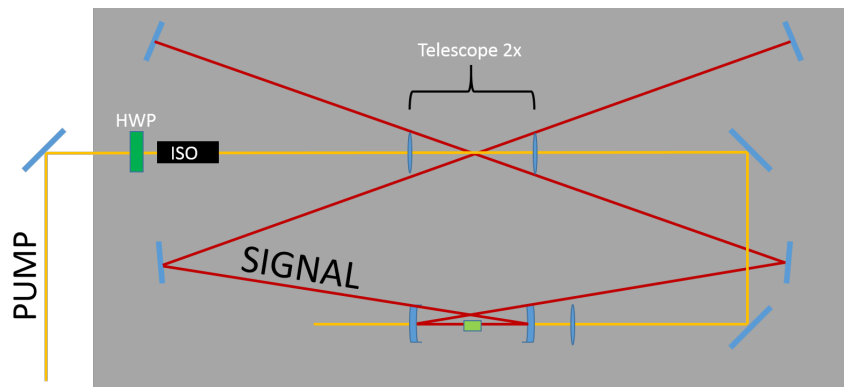
Figure 5.4: New configuration of the OPO source.

Figure 5.4 shows that the input stage (HWP, ISO, Telescope and Lens) is now on the breadboard without interfering with the Signal beam path. With this configuration the input stage optics are mounted on smaller pedestals (6.5 cm) than before (12.5 cm), ensuring a better stability. This solution has been implemented recently, Figure 5.5 shows the result.

Figure 5.5: Photo of the OPO cavity with the compact solution. In red is represented the Pump beam while in brown the Signal beam.

Appendix A

Alignment Procedure

The alignment procedure can be divided in two parts:

- *Input Pump beam alignment*

- *Resonator alignment*

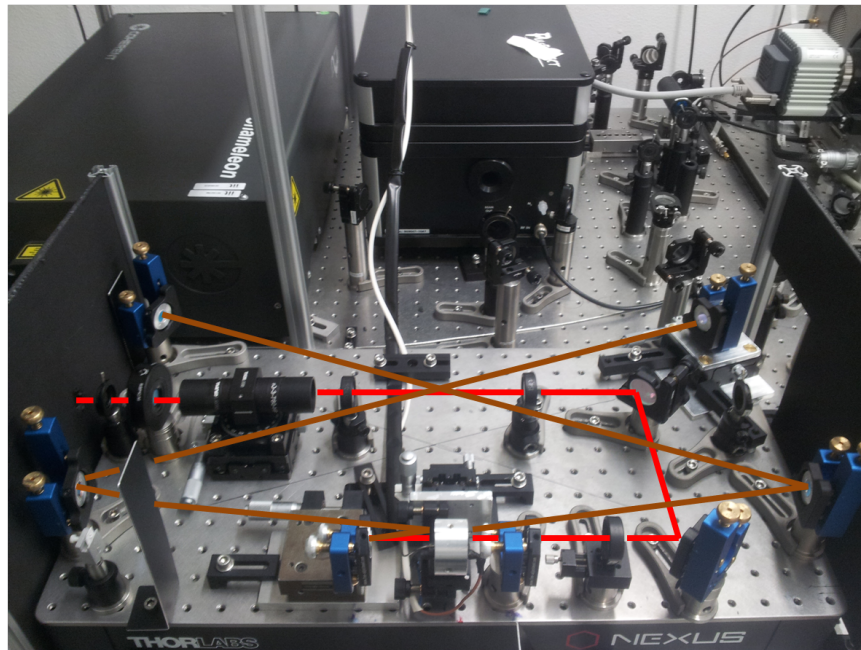The first part consists in aligning all the optical elements present before entering the resonator, the second part consists in aligning the cavity in order to obtain lasing.

A.1   Input

As with any alignment procedure it is good practice to ensure the input beam is traveling parallel to the surface of the optical table at a convenient height (here 125 mm), and is also traveling along a set of holes in the table which act as a convenient reference line. This was carried out using a pair of steering mirrors. It is also good practice to attenuate the Pump beam to reduce the potential both for damaging the optics as they are inserted into the beam line and for safety concerns. A sketch of the Input stage is shown in the Figure A.1.
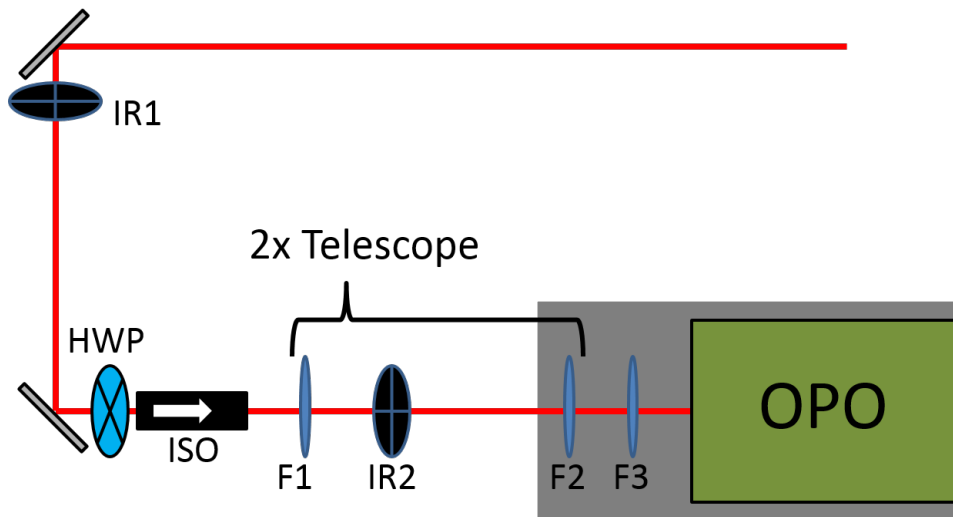
Figure A.1: Input Pump beam path before entering the cavity.

The following optical elements are listed in Figure A.1:

- Two steering mirrors

- Two irises (IR1 and IR2)

- An Half-Wave Plate (HWP)

- An optical isolator (ISO)

- A 2x telescope ($f_1 = 50mm$ and $f_2 = 100mm$)

- A lens of $f = 100mm$ for focusing the Pump into the crystal

- A 60 mm high Breadboard in gray where the OPO resonator was set

The beam exiting the Pump source was at an height of 120 mm, using the two steering mirrors a 125 mm height was obtained for the beam: this height was chosen because all the other optical elements present on the optical table were at that height. In order to be always aligned and at the right height two irises were put on the beam path, these elements will be the reference for aligning all the other optical elements.

After having put the irises, it was the turn of the HWP and of the ISO. The first step was to optimize the direction of the ISO polarizers in order to obtain an horizontal polarization of the Pump after the ISO itself. As it was mentioned in the Cavity Subsection of the Second Chapter, the Pump beam exiting the Chameleon source is horizontally polarized and after the sequence of the HWP and of the ISO must be horizontally polarized again. In order to obtain one of the two ISO polarizers exactly on the horizontal direction, the ISO was rotated until the transmitted power was optimized. This solution is supported by the fact that the Pump beam polarization it was already horizontal and it was used as a reference while aligning the ISO polarizers. In this way it was sure that one polarizer of the ISO was at 45° and the other was horizontal. Then it is important to set the right angle for the HWP crystal. In fact, before entering the ISO, a 45° precise polarization of the Pump beam (this is important in order to avoid losses of the Pump through the ISO) is needed. This was obtained by maximizing the Pump power after the HWP-ISO sequence while the angle of the HWP was varied (the ISO has the input polarizer at 45° and the output polarizer horizontal). All these procedures were done taking into account that the beam has to pass through the irises.

The remaining optical elements were put on the optical table, except the focusing lens, making sure that the distance between the two lenses of the telescope was right (150 mm) in order to obtain a collimated beam.

A.2   Resonator

The next step is to align the OPO resonator, taking into account that the focusing lens of the Input Part must be placed just before putting the crystal inside the resonator. The figure below shows the resonator's elements on their position on the 30x60cm breadboard.

In Figure A.2 M1 is the resonator's input mirror, M5 is the OC and M3/M4 are the folding mirrors. After the Input Part alignment is done, the Pump beam is horizontally polarized and is traveling straight at a height of 125 mm. It was decided to use a 60 mm high BreaBoard in order to avoid
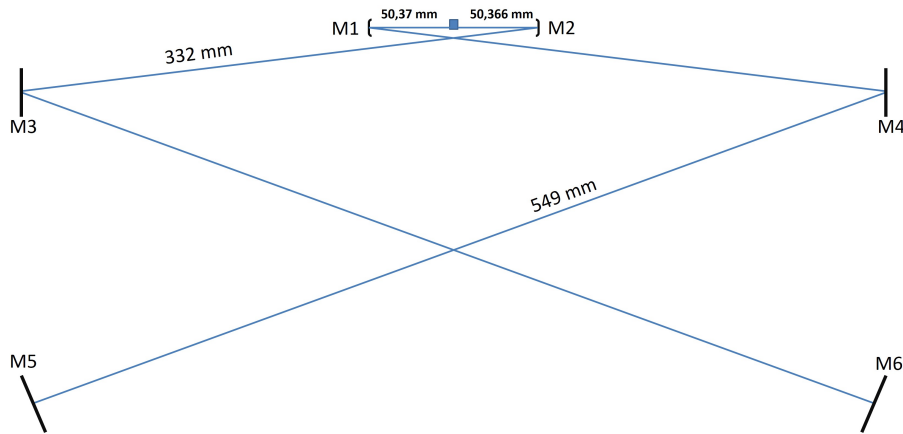
Figure A.2: Sketch of the resonator geometry in scale, having fixed a 30x60cm breadboard as the maximum space possible.

the use of high optical mounts that are very unstable; in this way the optical mounts were 65 mm high, allowing a better stability of the resonator in terms of mechanical vibrations.

The first step was to position the curved mirror M2, which was mounted on a translation stage that moved along the direction of the Pump beam. The height of the mirror mount was adjusted so that Pump beam was incident with the center of the half-inch mirror optic. The mirror mount assembly was then secure to the optical bench, leaving sufficient space for the crystal mount, for the second curved mirror and for the Pump lens assembly. A piece of white card was placed over mirror M2 and marked with a cross, so that the Pump beam fell on the center of the cross. This fixed reference was used to monitor how the Pump beam deviated as each additional element was added to the beam path.

The second step was to bring the input curved mirror M1 at about the right position relative to the center of the breadboard. It's important that the Pump beam has to pass through the center of both the two curved mirrors.

The third step was to position the Pump focusing lens. The lens had a focal length of 100 mm and was located on a translation stage. The Pump beam was blocked while the lens assembly was secured to the optical bench.

106

The Pump beam was then unblocked, producing a large spot on the piece of card attached to mirror M2. If the lens was correctly positioned in the horizontal and vertical direction relative to the Pump beam then this large spot was centered on the cross on the white card. The angular alignment of the lens was not critical; however it is good practice to align it orthogonally to the Pump beam to reduce losses. While these three steps are in action it is important to heat the crystal, in order to have it at the right temperature for the fourth step.

The fourth step was to bring the PPLN crystal into the correct position relative to the Pump curved mirrors. The crystal was orientated so that the two end-faces were as orthogonal as possible to the Pump beam. The translation stages of mirror M2 and of the crystal were then moved until the distance between the mirrors and the crystal surfaces were respectively 50,37 mm and 50,37 mm. This was achieved by cutting a piece of card to the correct length and tapering the ends to produce a measurement tool. Gently placing the card against the surface of the crystal, mirror M1/M2 was slowly brought into place until it touched the card. When the Pump is unblocked, after having selected a grating form the crystal, visible frequency doubling of the pump (780 nm) to its second harmonic (390 nm) is observed. The intensity of the second harmonic beam was increased by moving the focusing lens translation stage, and provided a good visual approximation of the position of the focal spot within the crystal. The angle of the crystal was altered until the Pump reflections from the crystal surfaces straddled the centers of the curved mirrors.

The final step was to place the resonator's mirrors M3, M4, M5 and M6 in the correct position. Matlab calculations had determined that the correct distance required to match the Pump cavity length was 1873 mm. In order to have a 6° angle between the mirror M1/M2 and mirror M3/M4 the optimal distance was calculated using the theorem of Pythagoras, taking into account the space available on the breadboard. Mirrors M5 and M6 were then placed at the right distance from mirrors M3 and M4 respectively. The white card was removed from mirror M2 and the blue SHG beam steered through the resonator's mirrors. A movable iris was then set inside the resonator in order

to align the coming-back rays from mirrors M5 and M6. The HR coating for the OPO mirrors and crystal input surface was sufficiently reflective at 390 nm that the generated SHG was visible for the round trip of the resonator. The blue beam was steered through the first arm of the resonator (mirrors M3 and M6), making sure with the movable pinhole that the beam was overlapping itself during the return trip of this arm. Before making the same alignment procedure on the other arm of the resonator (mirrors M4 and M5), it is important to overlap the blue ray coming back from the first arm with the Pump beam and the crystal reflection on mirror M1: this situation ensures that the beam is going straight in the resonator and that is spatially overlapped with the Pump. Now it's possible to proceed to the second arm alignment, checking that on mirror M5 the round-trip ray and the back-reflected ray from the first surface of the crystal are overlapped (can be monitored by blocking and opening in sequence the first branch of the resonator). At this point the attenuation was removed from the Pump beam and the iris was removed from beam line, noticeably increasing the SHG brightness.

The resonator's length could now be altered until oscillation occurred. The lab was darkened and the translation stage attached to M5 was moved. At the point of resonator's length synchronicity a flash of color could be observed: a result of various second harmonics and frequency mixing outputs between the Pump, Idler and resonant Signal beams. Once the correct resonator's length was established and the visible colors generated, the resonator's alignment was optimized by moving the beam using mirrors M5 and M6. Optimization was performed to maximize Signal output power using an optometer.

Bibliography

1. F. J. Duarte, *Tunable Laser Applications, Second Edition.* CRC Press, 2010.

2. A. Weiner, *Ultrafast Optics.* John Wiley and Sons, 2011.

3. J. A. Armstrong, N. Bloembergen, J. Ducuing, and P. S. Pershan, "Interactions between light waves in a nonlinear dielectric," *Phys. Rev.*, vol. 127, pp. 1918–1939, Sep 1962.

4. D. Finlayson and B. Sinclair, *Advances in Lasers and Applications.* Scottish Graduate Series, Taylor & Francis, 1999.

5. V. Ramaiah-Badarla, A. Esteban-Martin, and M. Ebrahim-Zadeh, "Self-phase-locked degenerate femtosecond optical parametric oscillator based on BiB_3O_6," *Laser and Photonics Reviews*, vol. 7, no. 5, pp. L55–L60, 2013.

6. E. C. Cheung and J. M. Liu, "Theory of a synchronously pumped optical parametric oscillator in steady-state operation," *J. Opt. Soc. Am. B*, vol. 7, p. 1385, Aug 1990.

7. H. Driel, "Synchronously pumped optical parametric oscillators," *Applied Physics B*, vol. 60, no. 5, pp. 411–420, 1995.

8. H. Rabin, *Quantum Electronics: A Treatise, Volume 1.* Elsevier, 1975.

9. C. McGowan, D. T. Reid, Z. E. Penman, M. Ebrahimzadeh, W. Sibbett, and D. H. Jundt, "Femtosecond optical parametric oscillator based on

periodically poled lithium niobate," *J. Opt. Soc. Am. B*, vol. 15, pp. 694–701, Feb 1998.

10. B. Denker and E. Shklovsky, *Handbook of Solid-State Lasers: Materials, Systems and Applications.* Woodhead Publishing Series in Electronic and Optical Materials, Elsevier Science, 2013.

11. R. McCracken, *Coherent synthesis of visible pulses generated by a PPKTP based Optical Parametric Oscillator.* PhD thesis, Heriot-Watt University, Edinburgh, 2013.

12. K. Fradkin, A. Arie, A. Skliar, and G. Rosenman, "Tunable midinfrared source by difference frequency generation in bulk periodically poled KTiOPO$_4$," *Applied Physics Letters*, vol. 74, pp. 2723–2723, May 1999.

13. O. Gayer, Z. Sacks, E. Galun, and A. Arie, "Erratum to: Temperature and wavelength dependent refractive index equations for MgO-doped congruent and stoichiometric LiNbO$_3$," *Applied Physics B*, vol. 101, no. 1-2, pp. 481–481, 2010.

14. T. Andres, P. Haag, S. Zelt, J.-P. Meyn, A. Borsutzky, R. Beigang, and R. Wallenstein, "Synchronously pumped femtosecond optical parametric oscillator of congruent and stoichiometric MgO-doped periodically poled lithium niobate," *Applied Physics B*, vol. 76, no. 3, pp. 241–244, 2003.

15. J. Fonseca-Campos, Y. Wang, W. Liang, C.-Q. Xu, and I. Vargas-Baca, "Comparison of photorefractive effects in undoped and MgO-doped PPLN," *Proc. SPIE*, vol. 6796, pp. 679619–679619–8, 2007.

16. B. Sturman, M. Aguilar, F. Agulló-López, V. Pruneri, and P. G. Kazansky, "Photorefractive nonlinearity of periodically poled ferroelectrics," *J. Opt. Soc. Am. B*, vol. 14, pp. 2641–2649, Oct 1997.

17. W. Shunhua, *Fabrication and characterization of periodically-poled KTP and Rb-doped KTP for applications in the visible and UV.* PhD thesis, Royal Institute of Technology Stockholm, Sweden, 2005.

18. Z. Zhang, J. Sun, T. Gardiner, and D. T. Reid, "Broadband conversion in an Yb:KYW-pumped ultrafast optical parametric oscillator with a long nonlinear crystal," *Opt. Express*, vol. 19, pp. 17127–17132, Aug 2011.

19. P. Loza-Alvarez, C. T. A. Brown, D. T. Reid, W. Sibbett, and M. Missey, "High-repetition-rate ultrashort-pulse optical parametric oscillator continuously tunable from 2.8 to 6.8 μm," *Opt. Lett.*, vol. 24, pp. 1523–1525, Nov 1999.

20. X. P. Zhang, J. Hebling, J. Kuhl, W. W. Rühle, and H. Giessen, "Efficient intracavity generation of visible pulses in a femtosecond near-infrared optical parametric oscillator," *Opt. Lett.*, vol. 26, pp. 2005–2007, Dec 2001.

21. O. Svelto, *Principles of Lasers, FOURTH EDITION*. Springer, 2010.

22. M. J. P. Alcocer, *Exploring light harvesting systems via broadband transient photoluminescence spectroscopy*. PhD thesis, Physic Department of Politecnico Di Milano, Milan, 2014.

23. R. Croce and H. Amerongen, "Light-harvesting in photosystem I," *Photosynthesis Research*, vol. 116, no. 2-3, pp. 153–166, 2013.

24. H. Amerongen and R. Croce, "Light harvesting in photosystem II," *Photosynthesis Research*, vol. 116, no. 2-3, pp. 251–263, 2013.

25. S. Boussiba, "Carotenogenesis in the green alga haematococcus pluvialis: Cellular physiology and stress response," *Physiologia Plantarum*, vol. 108, no. 2, pp. 111–117, 2000.

26. G. T. Kennedy, D. T. Reid, A. Miller, M. Ebrahimzadeh, H. Karlsson, G. Arvidsson, and F. Laurell, "Near- to mid-infrared picosecond optical parametric oscillator based on periodically poled $RbTiOAsO_4$," *Opt. Lett.*, vol. 23, pp. 503–505, Apr 1998.

27. M. Ebrahimzadeh, S. French, and A. Miller, "Design and performance of a singly resonant picosecond LiB_3O_5 optical parametric oscillator

synchronously pumped by a self-mode-locked Ti:sapphire laser," *J. Opt. Soc. Am. B*, vol. 12, pp. 2180–2191, Nov 1995.

28. M. J. McCarthy and D. C. Hanna, "All-solid-state synchronously pumped optical parametric oscillator," *J. Opt. Soc. Am. B*, vol. 10, pp. 2180–2190, Nov 1993.

29. L. E. Myers, R. C. Eckardt, M. M. Fejer, R. L. Byer, W. R. Bosenberg, and J. W. Pierce, "Quasi-phase-matched optical parametric oscillators in bulk periodically poled LiNbO$_3$," *J. Opt. Soc. Am. B*, vol. 12, pp. 2102–2116, Nov 1995.